applied sciences

MDPI

Article

Metering Pin Optimization and Spatial Tolerance Sensitivity in Articulated Aircraft Landing Gear

Kun Wang [1,*], Qinbo Zhang [1,2], Xie Zhao [1,2] and Wei Zhang [3]

[1] China Ship Scientific Research Center, Wuxi 214082, China
[2] Key Laboratory of Ship Structure Safety, Wuxi 214082, China
[3] Technical Institute of Physics and Chemistry, Chinese Academy of Sciences, Beijing 100190, China
* Correspondence: wangkun@cssrc.com.cn

Abstract

Metering-pin profiles govern stroke-dependent hydraulic resistance in articulated aircraft landing gear. This study combines multiobjective optimization, analytical diameter-error amplification and spatial sensitivity screening in a twin-wheel vertical-drop model. The model uses an initial absolute gas pressure of 2.95 MPa and defines load factor using a single-wheel static reference. The optimized pin gives a peak single-wheel load factor of 1.21447 over a 2 s response and first-compression energy-utilization efficiency of 95.302%, compared with 1.62791 and 57.268% for a constant pin. Both numerical design targets are met at the prescribed drop condition. Five independent optimization runs assess nominal performance. A 64-case ANSYS 2022 R1 design and 50,176 sensitivity evaluations quantify dimensional effects around the baseline profiled pin. The final-hypervolume coefficient of variation is 0.60%; extending the generation budget improves hypervolume by 0.210–1.200%, indicating remaining finite-budget search dependence. Main-effect and total-order estimates identify a leading station group near 140–170 mm, with uncertainty in detailed ordering. The results support conditional geometric screening. Assembly-specific drop tests and manufacturing-capability measurements are required before production tolerances or qualified landing performance can be established.

Keywords: articulated landing gear; oleo-pneumatic shock absorber; metering pin; multiobjective optimization; dimensional sensitivity; manufacturing tolerance

1. Introduction

An aircraft landing gear must distribute touchdown energy over limited travel while controlling the forces transmitted through the tires and airframe. In an oleo-pneumatic shock absorber, compressed gas stores energy and fluid flow through the metering restriction dissipates energy. The metering-pin profile changes the restriction as the strut compresses and therefore shapes damping throughout the landing event. Pritchard [1] reviewed landing-gear dynamic problems, including shimmy and brake-induced vibration.

Landing response depends on both the shock absorber and its mechanical arrangement. Krüger and Morandini [2] reviewed multibody methods for landing-gear dynamics, while Pecora [3] developed a compact numerical representation of oleo-pneumatic drop impact. More detailed strut models account for gas–oil heat exchange, chamber compliance, and gas dissolution [4]. Nonlinear finite-element impact models [5], elastic shock-

Academic Editor: Paolo Renna

Received: 27 September 2026
Revised: 2 November 2026
Accepted: 3 November 2026
Published: 4 November 2026

Copyright: © 2026 by the authors. Licensee MDPI, Basel, Switzerland. This article is an open access article distributed under the terms and conditions of the Creative Commons Attribution (CC BY) license.

absorber models [6], and flexible multibody models with bearing contact [7] extend the description of structural load transmission. These modeling choices make the geometry, joint definitions, and hydraulic interface essential parts of a reproducible analysis.

Articulated gear adds a rotating arm between the supported mass, wheel assembly, and shock absorber. The arm changes both strut travel and force transmission during compression. Consequently, the maximum shock-absorber force and the maximum tire force measure different aspects of performance. Model-based landing-gear design has increasingly combined preliminary sizing with dynamic assessment [8]. Experimental work on nose landing gear also shows the importance of distinguishing ground-contact loads from wheel-axle loads when comparing calculations with drop tests [9]. For an articulated arrangement, a design assessment should retain the arm dynamics and define the location of each reported force.

Studies of multi-strut assemblies illustrate how gear topology enters landing dynamics [10]. Drop-test rig development for light airplanes [11], impact-test comparisons for unmanned-aircraft gear [12], and tests of twin-tandem arrangements [13] further establish the importance of recording the supported mass, release condition, contact configuration, and measured force location. Those quantities provide the basis for interpreting comparisons between models and tests.

Pin optimization has progressed beyond selecting a single orifice diameter. Shi [14] compared passive metering-pin constructions using multiple objectives and variable supported mass. Dinç [15] optimized pin diameters using a genetic algorithm and a dynamic landing-gear model. Liu et al. [16] linked orifice-area configuration to the compression and extension behavior of a carrier-aircraft shock absorber. These studies establish the relevance of profiling the flow area throughout the stroke. They also show why the effectiveness of a profile must be judged through the complete force and motion response.

Semiactive landing-gear control [17] and magnetorheological-damper models [18] offer additional ways to adjust impact response. In a passive metering-pin design, the axial diameter distribution encodes stroke-dependent hydraulic resistance. Connecting that distribution to dimensional sensitivity allows nominal performance and prescribed geometric deviations to be examined within the same description.

Manufacturing variation adds a spatial question to that optimization problem. A diameter error at one axial position can have a different effect from an equal error elsewhere. Friction-related parameters can also alter touchdown performance [19], and detailed flow calculations show that orifice geometry affects damping and the internal flow field [20]. Tolerance studies of landing-gear retraction mechanisms have connected geometric deviations with functional accuracy [21]. Diagnostic models have addressed the condition of landing-gear subsystems [22], while recent lever-spring studies have combined multibody simulations with drop tests [23]. For the present oleo-pneumatic articulated gear, the useful design question is where dimensional control contributes most to the selected landing-performance objective.

This paper links metering-pin shape to landing performance and dimensional sensitivity within a twin-wheel dynamic model. The nondominated sorting genetic algorithm II (NSGA-II) [24] minimizes tire-load factor and maximizes first-compression energy utilization. Analytical hydraulic derivatives explain the local effects of diameter errors, while a 64-case numerical design identifies influential axial stations around the baseline profiled pin. Objective-weighted scores, conditional ranking diagnostics and interaction-aware sampling assess how those priorities depend on the response being controlled. Independent integration, time-step refinement and repeated optimization runs quantify numerical and algorithmic stability.

https://doi.org/10.3390/app162110943

2. Landing Gear Model and Design Definition

2.1. Mechanical Arrangement and Landing Condition

The gear is represented by an upper body, a rotating arm and a wheel assembly. The upper body contains the equivalent supported mass and the upper strut attachment. The arm connects the body to the wheel axle and carries the lower strut attachment. Two identical tires provide ground contact. Upper-body motion is restricted to the vertical direction, while the arm rotates about its pivot. The initial sink speed is 3.05 m/s and the initial arm angular velocity is zero. Horizontal tire forces, wheel spin and additional aerodynamic lift are omitted.

The aircraft reference mass is 26,300 kg. A fraction of 0.92 is assigned to two main-gear units with two wheels per unit, giving 6049 kg per wheel for static normalization. With gravitational acceleration 9.8 m/s^2, the rounded single-wheel reference force is 59,280 N. The two tire forces are summed in the equations of motion, whereas load factor is calculated from the force of one tire divided by this static reference.

The prescribed upper-body mass is 6261.17 kg; the arm and total wheel-assembly masses are represented separately. This dynamic input differs from the static mass used for single-wheel load normalization. The study does not establish a unique reduced-mass or aerodynamic-lift transformation from the complete aircraft to the prescribed drop condition. Performance targets are therefore assessed for the stated mass, sink speed and modeling assumptions.

A release from rest producing a sink speed of 3.05 m/s corresponds to a free-fall height of approximately 0.475 m. With unloaded tire radius 0.4318 m, the corresponding initial axle height is approximately 0.906 m. Time is measured from first tire contact; release-aligned time is obtained by adding 0.3112 s. The 203 mm empirical sizing value provides a stroke comparison and is not treated as an identified mechanical travel limit. Table 1 summarizes the model parameters, and Table 2 gives the baseline profiled-pin geometry.

Table 1. Model parameters and their roles in the twin-wheel calculation. Adopted mass, inertia, center-of-mass and environmental assumptions are specified in Section 2.

Quantity	Value	Use in the Study
Reference aircraft mass	26,300 kg	Static wheel-load normalization
Main-gear share and wheel count	0.92 and 4	Static mass of 6049 kg per wheel
Prescribed upper-body mass	6261.17 kg	Prescribed upper-body mass; see Section 2.1
Nominal sink speed	3.05 m/s	Selected vertical landing condition
Tire diameter and inflation pressure	863.6 mm and 145 psi	Pressure is approximately 1.00 MPa
Outer and inner cylinder diameters	150 and 135 mm	Full-bore gas area; annular hydraulic area
Metering-hole diameter	25.9 mm	Fixed during pin-profile optimization
Initial absolute gas pressure	2.95 MPa	Absolute pressure in the polytropic law
Initial gas volume	4.6 L	Baseline chamber volume
Gas polytropic exponent	1.3	Fixed gas-law approximation
Constant-pin diameter	22.2 mm	Reference geometry
Baseline-profile maximum compression	201.712 mm	First maximum for Table 2 baseline
Empirical stroke-check value	203 mm	Sizing comparison; not a mechanical limit
Full-response verification window	0–2 s after first contact	Adaptive integration; three representative designs
Arm mass	185 kg	Adopted model input
Total wheel-assembly mass	158 kg	Both wheels combined; adopted input
Arm moment of inertia about pivot	42 kg·m^2	Adopted pivot inertia
Wheel spin moment of inertia	9.5 kg·m^2	Not used; wheel spin is omitted
Arm pivot-to-wheel-axle length	0.588926 m	Magnitude of OA = (0.435, −0.397) m

Arm pivot-to-strut-attachment length	0.288434 m	Magnitude of OB = (0.275, −0.087) m
Strut initial length (fully extended)	0.821032 m	Includes 0.191752 m transverse offset
Single-wheel tire stiffness	960,000 N/m	Two identical tires in parallel
Single-wheel tire damping	20,000.648 N·s/m	Two identical normal-force laws
Tire friction coefficient	0.2	Not used; horizontal tire forces are omitted
Oil density	870 kg/m^3	Hydraulic force model
Discharge coefficient C_d	0.781907	Geometric relation; β = 25.9/135

Table 2. Baseline profiled-pin geometry used for dimensional screening and as a performance comparison design.

Axial Position (mm)	Diameter (mm)	Axial Position (mm)	Diameter (mm)
0	22.40	110	22.80
10	22.40	120	23.00
20	22.40	130	23.00
30	22.30	140	23.20
40	21.90	150	23.40
50	21.30	160	23.50
60	22.16	170	23.70
70	22.20	180	23.70
80	22.40	190	24.00
90	22.60	200	24.00
100	22.80	210	24.00

Figure 1 shows the assembly configuration, hydraulic restriction and mechanical–hydraulic coupling. Relative to arm pivot O, the initial projected wheel-axle and lower-strut coordinates are OA = (0.435, −0.397) m and OB = (0.275, −0.087) m. The upper strut attachment is C = (0.141, 0.700, 0.191752) m, retaining the transverse offset in the strut length. Vertical upper-body displacement and arm rotation define the two generalized coordinates. Arm mass 185 kg, total wheel-assembly mass 158 kg and pivot inertia 42 kg·m^2 are adopted inputs; the arm center of mass is assumed to lie halfway along OA.

Mechanical–fluid coupling exchanges strut motion and axial force [25]. Here, the equations are integrated as one coupled dynamic system: strut stroke and velocity determine the gas, hydraulic and extension-stop forces, which enter the mechanical balances. Each tire follows a unilateral Kelvin–Voigt law: its normal force is $\max(0, k_t\delta + c_t\dot{\delta})$ for tire compression $\delta \geq 0$, and zero for $\delta < 0$. The two identical tire forces act in parallel. The model is integrated from first contact and is implemented in ANSYS Mechanical APDL 2022 R1 (ANSYS, Inc., Canonsburg, PA, USA) and independent ordinary differential equation (ODE) solvers. Numerical verification and complete 2 s responses of the three comparison designs are reported in Sections 4.3 and 4.9. Here, APDL denotes Ansys Parametric Design Language, and MAPDL denotes Mechanical APDL.

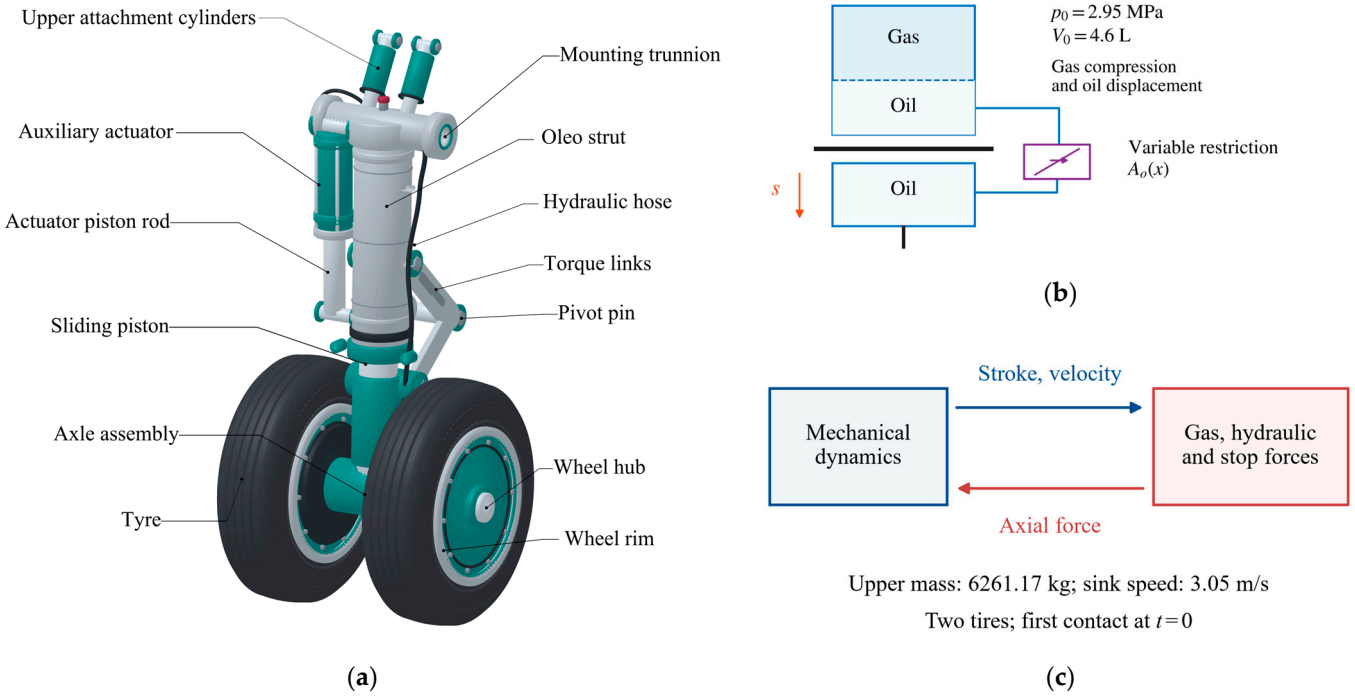


Figure 1. Assembly configuration and mechanical–hydraulic coupling. (**a**) Three-dimensional assembly geometry. (**b**) Functional gas chambers and metering restriction. (**c**) Exchange of strut motion and axial force in the numerical model, with the prescribed vertical-drop inputs. The two-coordinate dynamics are implemented using ANSYS Mechanical APDL (MAPDL; APDL, Ansys Parametric Design Language) and ordinary differential equation (ODE) solvers.

2.2. Planar Dynamics and Shock-Absorber Kinematics

For body i, the position of an attachment point P is written as

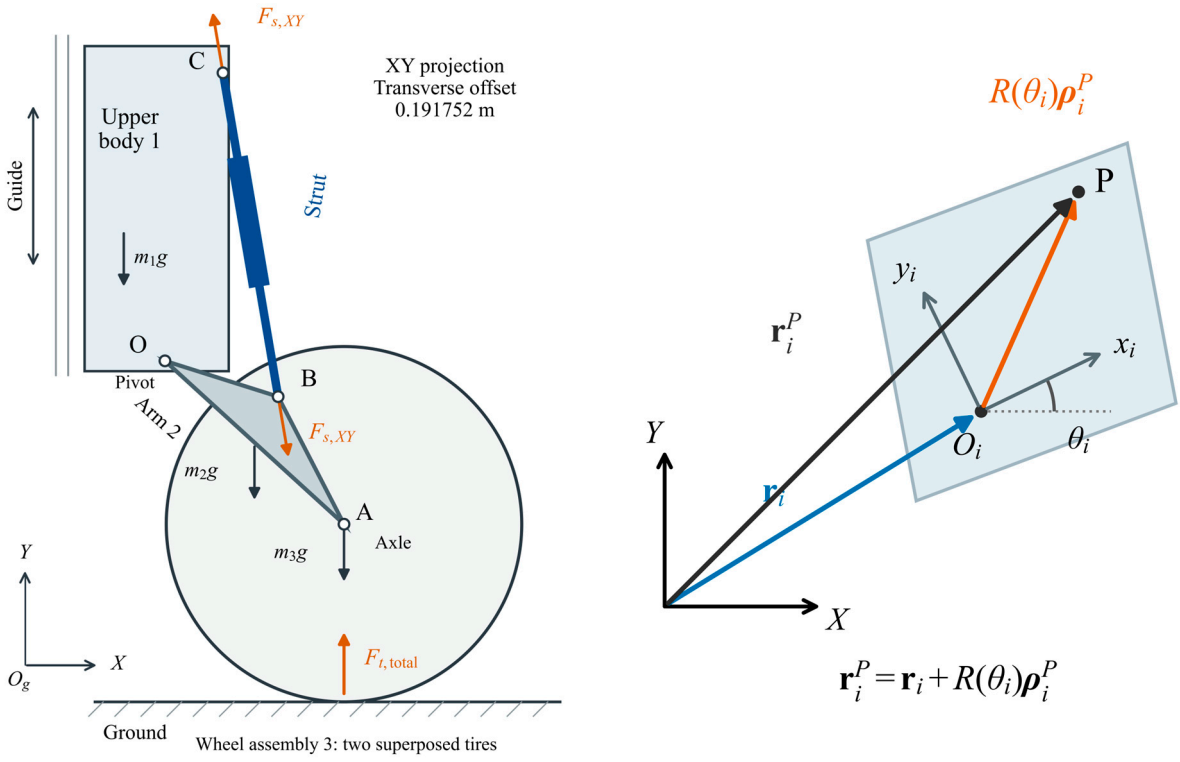
$$\mathbf{r}_i^P = \mathbf{r}_i + \mathbf{R}(\theta_i)\boldsymbol{\rho}_i^P, \qquad \mathbf{R}(\theta_i) = \begin{pmatrix} \cos\theta_i & -\sin\theta_i \\ \sin\theta_i & \cos\theta_i \end{pmatrix}. \tag{1}$$

Here, $\mathbf{r}_i$ is the body reference position, θ_i is its planar rotation, and $\boldsymbol{\rho}_i^P$ is the fixed attachment vector in the body frame. The planar force and moment balances for the three bodies, together with their joint constraints, can be assembled as

$$\mathbf{M}(\mathbf{q})\ddot{\mathbf{q}} + \boldsymbol{\Phi}_\mathbf{q}^T\boldsymbol{\mu} = \mathbf{Q}(\mathbf{q}, \dot{\mathbf{q}}), \qquad \boldsymbol{\Phi}(\mathbf{q}) = \mathbf{0}. \tag{2}$$

The generalized coordinates are collected in $\mathbf{q}$, the joint constraints in $\boldsymbol{\Phi}$, and the constraint reactions in $\boldsymbol{\mu}$. The force vector includes gravity, strut force, and tire-ground contact. Retaining the arm as a separate body preserves its rotational inertia and the change in force transmission during compression.

Figure 2 defines the coordinate and force conventions used in Equations (1)–(4). The global vertical coordinate is positive upward and gravity acts downward. Body-frame attachment vectors are rotated into the global frame. The axial strut force acts along the attachment line with equal and opposite forces on the connected bodies, and the summed normal tire force acts vertically upward through the wheel axle.



(**a**) (**b**)

Figure 2. (**a**) Projected geometry and force conventions: O is the arm pivot, A the wheel axle, B the lower strut attachment and C the upper attachment. The two identical tires coincide in this projection; Ft,total is their summed normal force, and Fs,XY denotes the in-plane projection of axial strut force. The 0.191752 m transverse strut offset is retained in Equation (3). (**b**) Global and body-frame coordinates and the transformation defining an attachment-point position.

Let $\mathbf{h}$ be the separation of the projected strut attachments and $\ell_\perp$ their fixed transverse offset. Positive stroke denotes compression. The strut length, stroke, and stroke velocity follow from

$$\ell = \sqrt{\mathbf{h}^T\mathbf{h} + \ell_\perp^2}, \qquad s = \ell_0 - \ell, \qquad \dot{s} = -\frac{\mathbf{h}^T\dot{\mathbf{h}}}{\ell}. \tag{3}$$

The axial strut force is resolved along the attachment direction before entering the body balances. Consequently, strut compression differs from the wheel axle's vertical displacement. An elastic extension stop defines the force balance near full extension. The pin interpolation law is specified over 0–210 mm, and integration terminates if its upper compression-domain bound is exceeded. This domain does not identify the mechanical bottoming travel.

2.3. Hydraulic Resistance and Gas Force

The total axial strut force combines net gas force F_g, hydraulic resistance F_h and the opposing extension-stop force F_{stop}:

$$F_s = F_g + F_h - F_{stop} \tag{4}$$

For a circular metering hole with diameter D_o and local pin diameter $d(s)$, the annular flow area A_o, displaced-fluid area A_h, and gas-force area A_g are

$$A_o = \frac{\pi}{4}(D_o^2 - d^2), \qquad A_h = \frac{\pi}{4}(D_2^2 - d^2), \qquad A_g = \frac{\pi}{4}D_1^2. \tag{5}$$

In Equations (5) and (6), D_1 = 150 mm and D_2 = 135 mm denote the cylinder diameters, D_o = 25.9 mm is the metering-hole diameter, ρ is oil density, and C_d is the discharge coefficient. Areas are expressed in m² after conversion from millimeters; R_h has units N·s²/m². Equation (5) gives the full-bore gas area A_g = 0.01767146 m².

The hydraulic resistance is quadratic in the stroke velocity,

$$F_h = \frac{\rho A_h^3}{2C_d^2 A_o^2}\dot{s}|\dot{s}| = R_h(d)\dot{s}|\dot{s}|. \tag{6}$$

The discharge coefficient is calculated as $C_d = 0.8\beta^2 - 0.4813\beta + 0.8448$, with β = 25.9/135, giving 0.781907. This value is held fixed during profile optimization and dimensional screening. In analytical diameter-error ratios, oil density, hole diameter, chamber diameter and C_d cancel; both A_o and A_h remain functions of pin diameter.

The gas-force formulation uses the polytropic pressure term,

$$p_g = p_0\left(\frac{V_0}{V_0 - A_g s}\right)^{\nu}, \qquad F_g = A_g(p_g - p_b), \qquad K_g = \frac{\mathrm{d}F_g}{\mathrm{d}s} = \frac{\nu A_g^2 p_g}{V_0 - A_g s}. \tag{7}$$

In Equation (7), p_0 = 2.95 MPa and p_g are absolute pressures, V_0 is initial gas volume, ν is the polytropic exponent and K_g is tangent gas stiffness. The assumed external back pressure is p_b = 0.101325 MPa and remains constant; the remaining gas volume must be positive. The extension-stop force is F_{stop} = max(0, $F_g0 - K_{stop}$ s), where $F_g0 = A_g(p_0 - p_b)$ and $K_{stop} = 10^8$ N/m. It balances the initial net gas force of 50.3402 kN and releases after 0.503402 mm compression. Its initial stored energy of 12.6707 J is included in the energy balance. Bearing friction is omitted, and thermal, frictional and detailed internal-flow effects remain modeling limitations [4,19,20]. The gas-law curves for V_0 = 4.2, 4.4 and 4.6 L are constitutive comparisons, not separate landing simulations.

2.4. Performance Objectives and Pin Parameterization

The dimensionless tire-load factor N is the maximum single-wheel vertical tire force over a stated time window divided by $F_{t,\mathrm{static}}$ = 59,280 N. Optimization, 64-case screening and global sensitivity analysis use the interval from first contact to first maximum strut compression. A separate 0–2 s integration evaluates the full response of the constant pin, baseline profiled pin and optimized pin; its load factor is identified explicitly. First-compression energy-utilization efficiency η is the axial strut work up to s_{max} divided by the rectangle of width s_{max} and height $F_{s,max}$:

$$N = \frac{\max_t F_t(t)}{F_{t,\mathrm{static}}}, \qquad \eta = \frac{\int_0^{s_{\max}} F_s(s)\,\mathrm{d}s}{F_{s,\max} s_{\max}}. \tag{8}$$

The force maximum $F_{s,max}$ and maximum compression s_{max} are taken over the same first-compression branch. The numerator is the work done on the strut during that branch, and the denominator is the work that a constant force equal to the branch maximum would perform over the same travel. Thus, η describes how uniformly the available force–stroke envelope is used. It includes gas compression work as well as dissipative work and does not equal the fraction of landing energy irreversibly dissipated in the fluid.

The pin is defined at 22 nodes from 0 to 210 mm in increments of 10 mm, giving 21 interpolation intervals. The diameter within interval i is

$$d(s) = d_i + \frac{s - x_i}{x_{i+1} - x_i}(d_{i+1} - d_i), \qquad x_i \le s \le x_{i+1}. \tag{9}$$

Here, d_i and d_{i+1} are constant nodal diameters at fixed axial coordinates x_i and x_{i+1}. The function $d(s)$ is the continuous piecewise-linear profile evaluated at the section encountered at stroke s. Equation (9) gives its restriction to interval i. When the same profile is plotted against the geometric axial coordinate x, it is denoted $d(x)$.

https://doi.org/10.3390/app162110943

The search minimizes $(N, 1-\eta)$ with all 22 node diameters bounded between 20 and 25 mm. NSGA-II uses a population of 100, 200 evaluated generations, crossover probability 0.9 and mutation probability 0.125 per variable [24]. The design targets are $N \leq 1.9$ and $\eta \geq 0.80$. These targets assess the designs after optimization and are not imposed as nonlinear feasibility constraints. The 203 mm empirical sizing value provides a separate stroke comparison.

Each candidate is a real-valued vector of 22 nodal diameters. Objective evaluation integrates the twin-wheel equations of motion through first maximum strut compression and returns N and η. Parent selection uses binary tournaments based on nondomination rank and crowding distance. Simulated-binary crossover and polynomial mutation generate offspring. Elitist environmental selection retains candidates from the combined parent and offspring population by rank and crowding distance [24]. Optimization settings, admissibility outcomes and numerical checks are reported in Section 4.10.

Table 2 defines the baseline profiled pin used for dimensional screening and performance comparison. Five independently seeded optimization runs provide nondominated sets for the same model (Figure 3). The optimized pin is selected from their pooled nondominated points by minimum Euclidean distance to the componentwise ideal after ideal-to-nadir scaling. The selection of the optimized pin and convergence diagnostics are discussed in Section 4.10. Performance of the three comparison designs is summarized in Table 3.

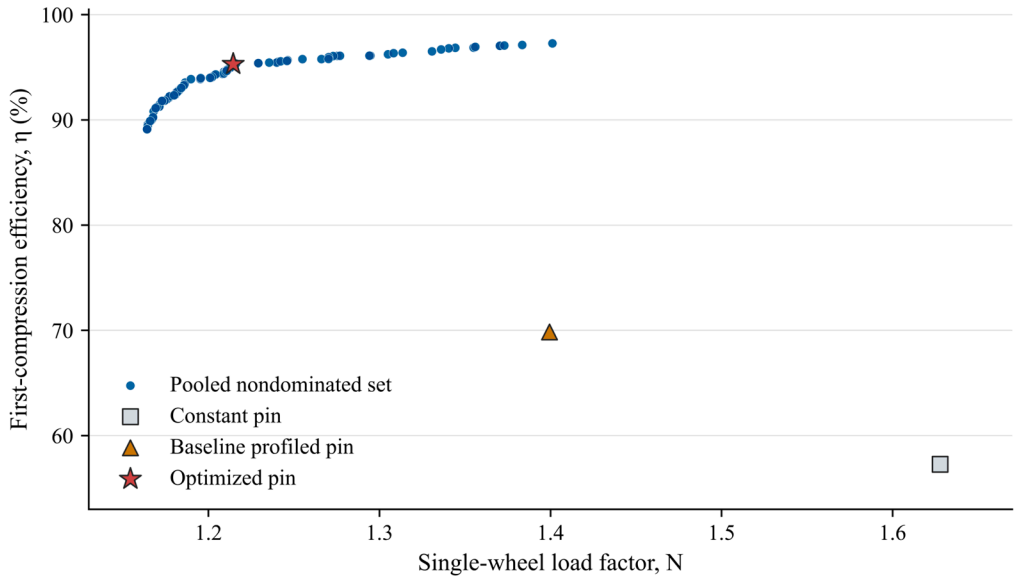


Figure 3. Nondominated objective values pooled from five 200-generation runs. Blue points show 91 pooled solutions evaluated by fourth-order Runge–Kutta (RK4) integration at 0.1 ms; symbols show independent eighth-order Dormand–Prince (DOP853) results for the constant pin, baseline profiled pin and optimized pin. Both objectives use the first-compression window. Integration differences are assessed in Section 4.10; 0–2 s design comparisons are reported separately in Table 3.

Table 3. Performance of the three pin designs under the prescribed twin-wheel drop condition. N uses the single-wheel tire force and a 59,280 N denominator; η and s_{max} refer to first strut compression. The 0–2 s load factor is evaluated separately for each design.

Quantity	Constant Pin	Baseline Profiled Pin	Optimized Pin
Peak N, first compression	1.627804	1.399416	1.214471
Peak N, 0–2 s	1.627914	1.399753	1.214471
First-compression efficiency (%)	57.268	69.842	95.302
First-compression stroke (mm)	208.147	201.712	187.646

0–2 s N change from constant pin (%)	0	−14.01	−25.40

Table 2 specifies the axisymmetric baseline pin. For circular, concentric pin and hole sections, radial clearances at 50, 100 and 190 mm are 2.30, 1.55 and 0.95 mm, respectively. The profile defines the stroke-dependent annular restriction in the articulated landing-gear model.

3. Spatial Sensitivity Analysis

3.1. Dimensional Screening and Comparable Factor Scores

The dimensional study perturbs 21 baseline node diameters from 0 to 200 mm and holds the 210 mm endpoint fixed. Each diameter is evaluated at its nominal value and at deviations of −0.2 and +0.2 mm. A node can affect the trajectory through an adjacent interpolation interval before its axial position is reached. Baseline maximum compression slightly exceeds 200 mm, so the fixed 210 mm endpoint participates in the final interpolation interval. Holding it fixed is a choice of screening variables, not a claim that it is physically inactive.

The ±0.2 mm amplitude is an illustrative perturbation amplitude chosen to compare equal absolute deviations at different stations; it spans approximately 0.83–0.94% of the nominal diameters in Table 2, but no drawing tolerance or machining-capability data are cited to establish it as a representative production tolerance. A diameter deviation changes radial clearance by half that amount. The present study does not represent circularity, cylindricity, straightness, concentricity, surface roughness or correlated profile errors; these can alter local clearance, flow separation, friction and wear even at the same measured diameter.

The 64-run design is constructed from an $L_{64}(4^{21})$ array by mapping the fourth level to the nominal level. Under this mapping, each factor has 32 nominal occurrences, 16 negative deviations, and 16 positive deviations. It is a collapsed four-level design with unequal three-level frequencies. A deterministic computer-experiment interpretation is appropriate for these calculations [26]. The 64 outputs describe the investigated parameter combinations; their distribution does not specify a manufacturing probability distribution.

Two sets of analysis of variance (ANOVA) statistics are reported. The marginal model groups the same 64 responses by one factor at a time. The adjusted model includes all 21 three-level main effects. These are analyses of the same multifactor study. With an intercept and two degrees of freedom per factor, the additive adjusted model has $64 - 1 - 42 = 21$ residual degrees of freedom. A marginal model has 61 residual degrees of freedom.

The 21 nodes define 210 factor pairs. Resolving all three-level two-factor interactions would require 840 additional parameters, exceeding the 21 residual degrees of freedom. Adjacent diameters jointly determine the interpolated restriction and subsequent motion, so the additive scores may depend on unmodeled interactions. Conditional fixed-design residual reallocation and leave-one-case-out fits assess ranking stability, while the input-sampling analysis in Section 4.11 evaluates total-order influence and interaction-sensitive prediction.

Let $F_{i,y}$ denote the adjusted ANOVA F statistic for diameter node i (i = 0, …, 20) and response y, where y is N or η. This statistic is the factor mean square divided by the common residual mean square and is distinct from physical force. The normalized adjusted score is

$$w_{i,y} = \frac{F_{i,y}}{\sum_{j=0}^{20} F_{j,y}}. \quad (10)$$

Each factor has two numerator degrees of freedom, and the adjusted statistics for a response share the same residual mean square. Equation (10) therefore gives each factor's share of the sum of main-effect sums of squares. The corresponding partial effect size is [27]

$$\eta_{p,i,y}^2 = \frac{2F_{i,y}}{2F_{i,y} + 21}. \tag{11}$$

The normalized score ranks axial positions within the screening design. Partial effect size compares a factor contribution with that contribution plus the residual. Variance-based global indices use a different decomposition and input-sampling scheme [28,29]. Elementary-effects methods provide another approach to computational screening [30,31]. Here, the main-effect statistics of the 64-case design provide the local station scores; total-order indices provide a complementary assessment under the explicitly assumed input distribution.

3.2. Analytical Amplification of Diameter Errors

At fixed stroke velocity, differentiation of the hydraulic-force law (Equations (5) and (6)) gives the local logarithmic diameter gain,

$$G_d = \frac{\partial \ln |F_h|}{\partial \ln d} = \frac{4d^2}{D_o^2 - d^2} - \frac{6d^2}{D_2^2 - d^2}. \tag{12}$$

The first term represents the reduction in annular flow area as the pin grows. The second accounts for the simultaneous reduction in displaced-fluid area. For a small diameter error e, the first-order relative force change is $G_d e/d$. The finite-error expression retains the full nonlinearity,

$$\frac{F_h(d+e)}{F_h(d)} = \left(\frac{D_2^2 - (d+e)^2}{D_2^2 - d^2}\right)^3 \left(\frac{D_o^2 - d^2}{D_o^2 - (d+e)^2}\right)^2. \tag{13}$$

The expression applies while the perturbed pin remains smaller than the metering hole. It measures local hydraulic-force sensitivity under the same velocity and fluid conditions. A complete perturbed landing would also change the stroke-velocity history and the arm motion. Keeping these two levels of sensitivity separate makes the geometric calculation useful for interpreting, rather than replacing, the system-level screening.

Throughout Equations (12) and (13), the analytical error plots and the nomenclature, e denotes a signed deviation of pin diameter. Positive e increases the diameter and decreases radial clearance by *e*/2, whereas negative e has the opposite effect. Both d and e must use the same length unit in Equation (13). The error may be evaluated locally at one section. A uniform-error curve applies the same prescribed offset to each section for comparison.

3.3. Objective-Dependent Screening Priority

A screening-priority score combines the two normalized response scores,

$$J_i(\lambda) = \lambda w_{i,N} + (1-\lambda) w_{i,\eta}, \qquad 0 \le \lambda \le 1. \tag{14}$$

Here, $\lambda = 1$ emphasizes load-factor control, $\lambda = 0$ emphasizes efficiency, and $\lambda = 0.5$ assigns equal weight to the normalized response scores. The scores sum to one. Sorting J_i identifies the positions accounting for the largest shares of the selected priority. Intersections of the linear functions identify any weight-dependent changes in order. The resulting priorities are conditional on the model and perturbation design. Dimensional acceptance limits would additionally require permitted performance deviations, measured process capability and a validated model of manufacturing errors.

4. Results

4.1. Pin Profile and Nonlinear Hydraulic Shaping

The baseline pin has a smaller-diameter region around 50 mm and a larger-diameter tail (Table 2). The former provides a larger annular flow area, while the latter progressively restricts the flow. This geometry redistributes hydraulic resistance during compression: the early opening reduces resistance, and the later restriction contributes to arresting the supported mass.

At the same stroke velocity, the hydraulic resistance at a 21.3 mm diameter is 0.676 times the constant-pin value, whereas the resistance at 24.0 mm is 3.474 times that value (Figure 4a). These local ratios explain how the profile reshapes the restriction encountered by the compressing landing-gear strut. They are not ratios of peak tire loads, because stroke velocity, tire deformation and arm transmission also evolve during the impact.

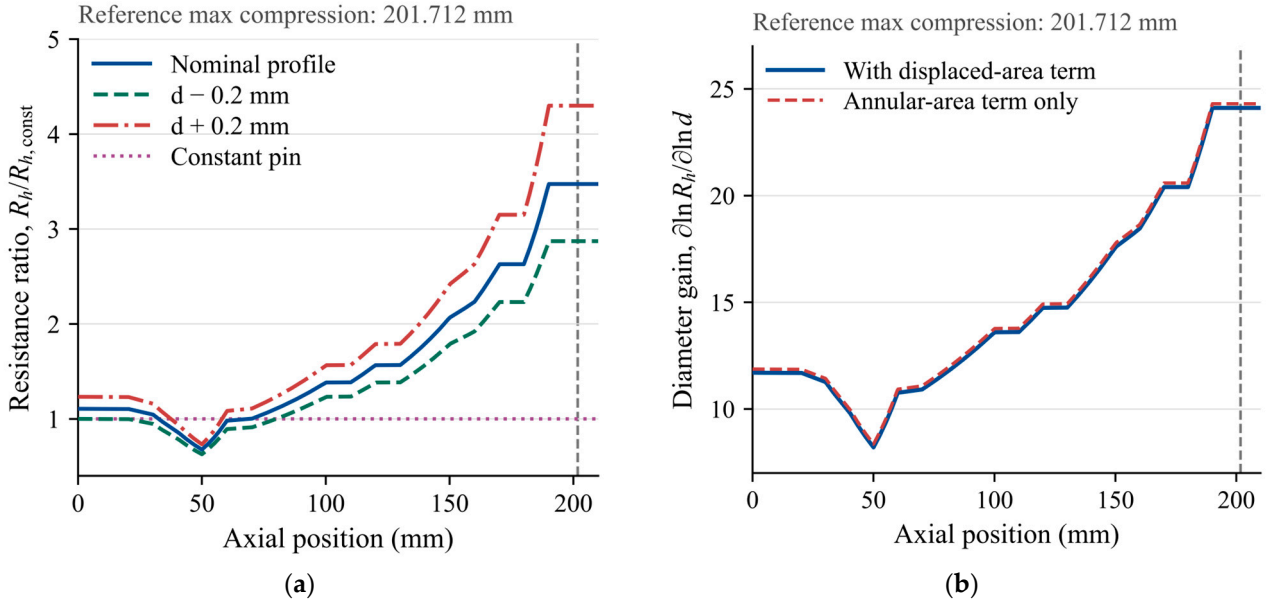


Figure 4. Conditional hydraulic response of the baseline profiled pin. (**a**) Hydraulic-resistance ratio relative to the constant 22.2 mm pin, for the baseline geometry and uniform diameter offsets. (**b**) Logarithmic diameter gain with and without the displaced-area term. The vertical marker at 201.712 mm indicates baseline maximum strut compression, not total pin length or an identified mechanical travel limit.

The logarithmic diameter gain increases from 8.21 at 21.3 mm to 24.11 at 24.0 mm (Figure 4b). The displaced-area term is small for this geometry, but retaining it keeps the derivative consistent with the hydraulic-force law. The high gain at the narrow tail passage identifies a region where a positive diameter deviation could substantially amplify the local hydraulic force; its contribution to the peak tire load must still be assessed through the coupled landing response.

4.2. Gas Response and Compression-Energy Utilization

Reducing the remaining gas volume raises absolute pressure and tangent stiffness nonlinearly. At a given stroke, the 4.6 L chamber retains more gas volume than the 4.2 and 4.4 L alternatives, reducing both pressure and stiffness near maximum compression (Figure 5a,b). These direct evaluations of Equation (7) describe the constitutive gas response; system-level changes in tire load would require integrating the coupled dynamics for each chamber volume.

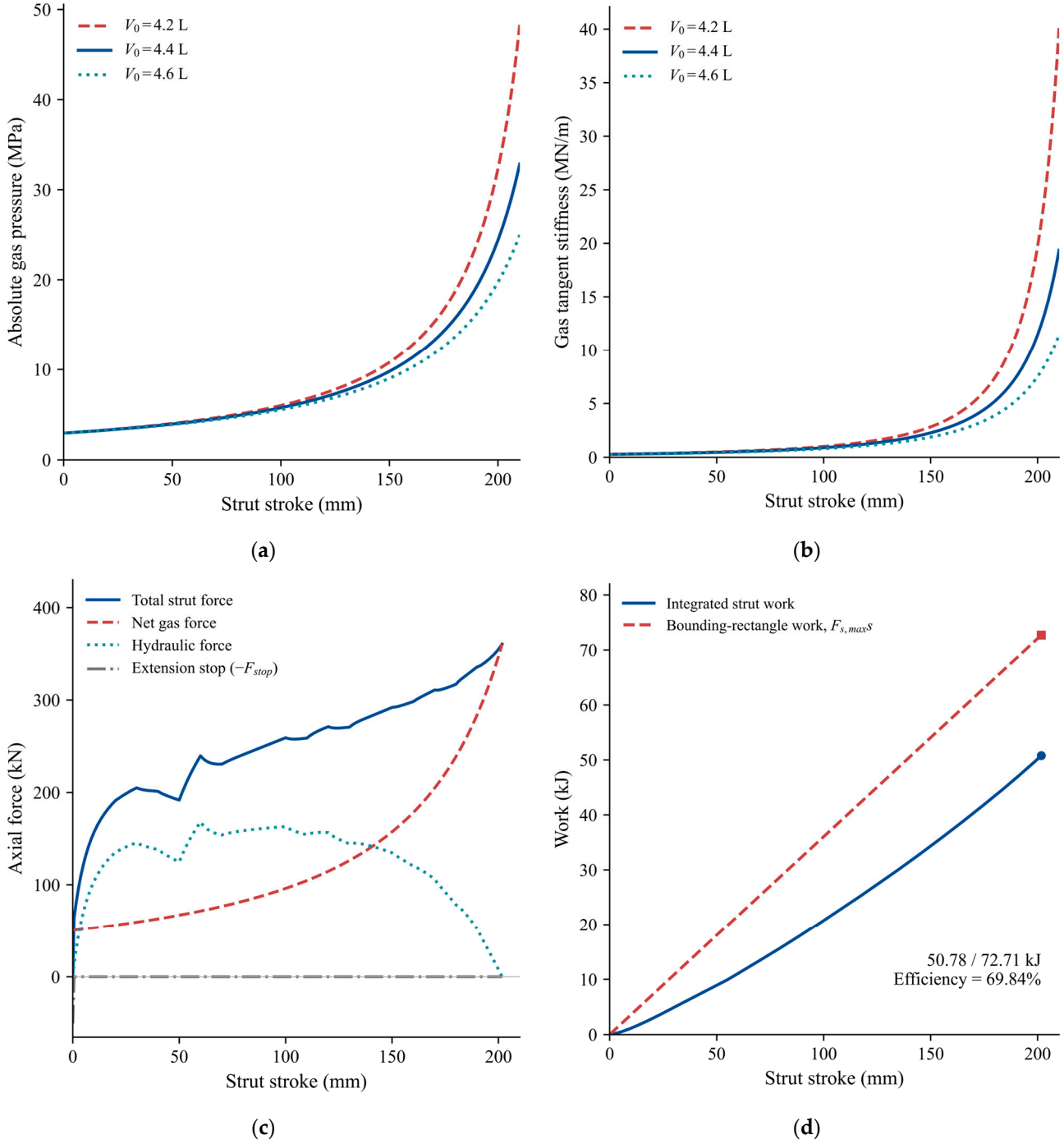


Figure 5. Gas response and baseline-pin compression work. (**a**) Absolute gas pressure and (**b**) tangent stiffness for three initial volumes at p_0 = 2.95 MPa absolute and ν = 1.3. (**c**) Total axial strut force and its net gas, hydraulic and opposing extension-stop components for the baseline profiled pin. (**d**) Integrated strut work and the force–stroke bounding rectangle. Panels (**c**,**d**) extend through first maximum strut compression.

For the baseline profiled pin, first maximum strut compression is 201.712 mm, peak axial force is 360.460 kN and integrated strut work is 50.781 kJ. The force–stroke bounding rectangle is 72.709 kJ, giving η = 69.842% (Figure 5c,d). The force components and integrated work are evaluated from the same dynamic trajectory and gas-pressure convention.

Strut work includes net gas-compression work and hydraulic dissipation, together with the explicitly modeled stop contribution. High η indicates use of the force–stroke

envelope rather than irreversible damping efficiency. The articulated mechanism transmits axial strut force to two tire contacts, so axial and single-wheel tire forces are different physical quantities. First-compression efficiency also remains distinct from rebound behavior or whole-event energy dissipation.

4.3. Nominal Performance and Transient Response

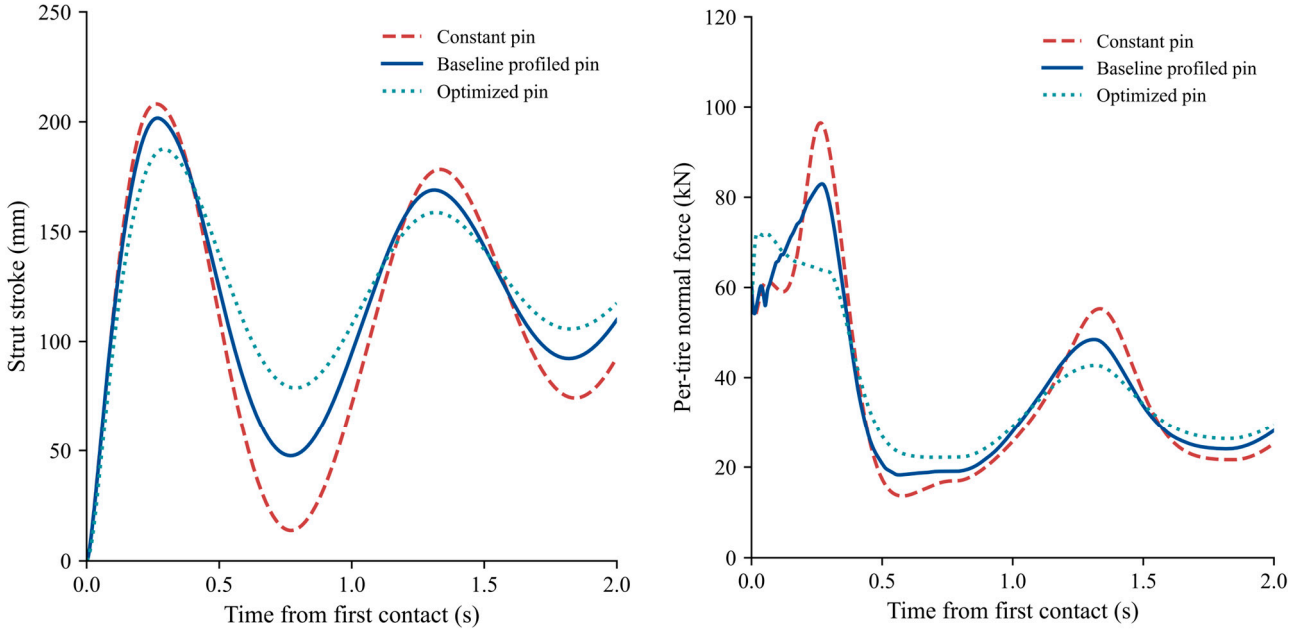
Table 3 compares the constant pin, baseline profiled pin and optimized pin under identical model inputs. Relative to the constant pin, the optimized pin reduces the 0–2 s single-wheel load factor by 25.40% and increases first-compression efficiency by 38.03 percentage points. Relative to the baseline profiled pin, the corresponding changes are 13.24% and 25.46 percentage points. The optimized pin satisfies $N \leq 1.9$ and $\eta \geq 0.80$ at the prescribed drop condition. The constant and baseline profiled pins satisfy the load target but not the efficiency target.

The compression-window load factors are 1.627804, 1.399416 and 1.214471, whereas the corresponding 0–2 s values are 1.627914, 1.399753 and 1.214471. The small increases for the first two profiles arise because their tire-force peaks occur shortly after maximum strut compression. The complete-response check therefore avoids equating a first-compression objective with a whole-record peak. The 210 mm profile domain and 203 mm sizing comparison do not establish the mechanical bottoming margin.

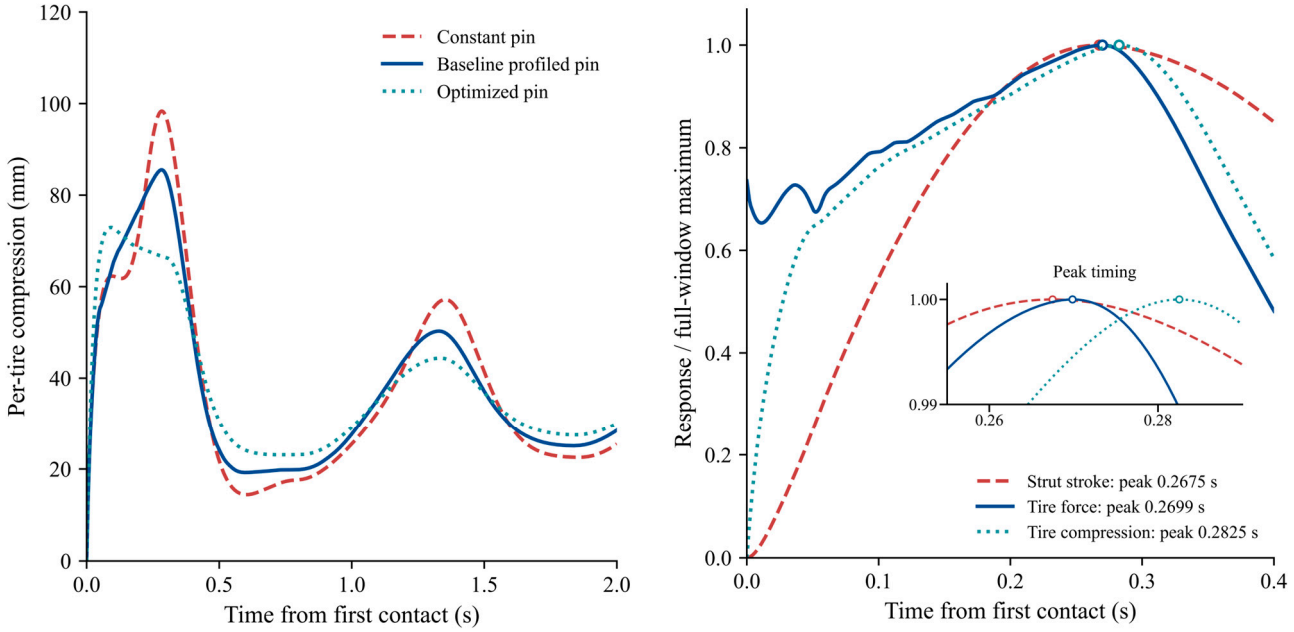
The three designs are evaluated with independent eighth-order Dormand–Prince (DOP853) and Radau integrations, time-step refinement and mechanical balance residuals. Section 4.9 reports the numerical verification procedures and results.

Figure 6 shows the complete 2 s response of the three designs. For the baseline profiled pin, maximum strut compression occurs at 0.267506 s, peak single-wheel tire force of 82.977 kN occurs at 0.269868 s, and maximum single-wheel tire compression of 85.540 mm occurs at 0.282535 s. Force and deformation peaks are distinct interior extrema, consistent with the elastic and damping contributions to tire force.

Panel (d) compares the baseline response components over the first 0.4 s, normalized by their respective 0–2 s maxima. The nonzero initial tire force follows from the Kelvin–Voigt damping term at first contact. Both tires remain in contact throughout the three 2 s trajectories. Independent-integrator agreement and a half-step check quantify numerical consistency; physical accuracy of the assumed contact law requires experimental assessment.



(**a**) (**b**)



(**c**) (**d**)

Figure 6. Twin-wheel landing responses. (**a**) Strut stroke, (**b**) single-wheel tire force and (**c**) single-wheel tire compression over 0–2 s after first contact for the constant pin, baseline profiled pin and optimized pin. (**d**) Baseline response components during the first 0.4 s, normalized by their respective full-record maxima.

4.4. Variability over the 64 Screening Cases

Across the 64 prescribed diameter combinations, first-compression load factor ranges from 1.36935 to 1.43174, efficiency from 67.876% to 71.705%, and maximum strut compression from 200.707 to 202.721 mm (Figure 7). These cases perturb the baseline profiled pin using the design in Section 3.1 and are evaluated with the same twin-wheel force and motion definitions.

Both objectives vary on either side of the unperturbed baseline within the screening design. Relative load-factor changes range from −2.193% to +2.263%, while relative efficiency changes range from −2.756% to +2.730%. These ranges describe the 64 investigated combinations and are not worst-case bounds over all possible profile deviations. Their joint distribution motivates considering both objectives when assigning station priorities.

The unperturbed baseline is case R001 in the MAPDL campaign, with N = 1.400056 and η = 69.7993%. Figure 7 uses this case as the reference for relative changes, keeping each comparison within the same discretization. The small differences from the high-accuracy baseline values in Table 3 are assessed by the solver and time-step checks in Section 4.9. The case-index plots preserve the declared design ordering.

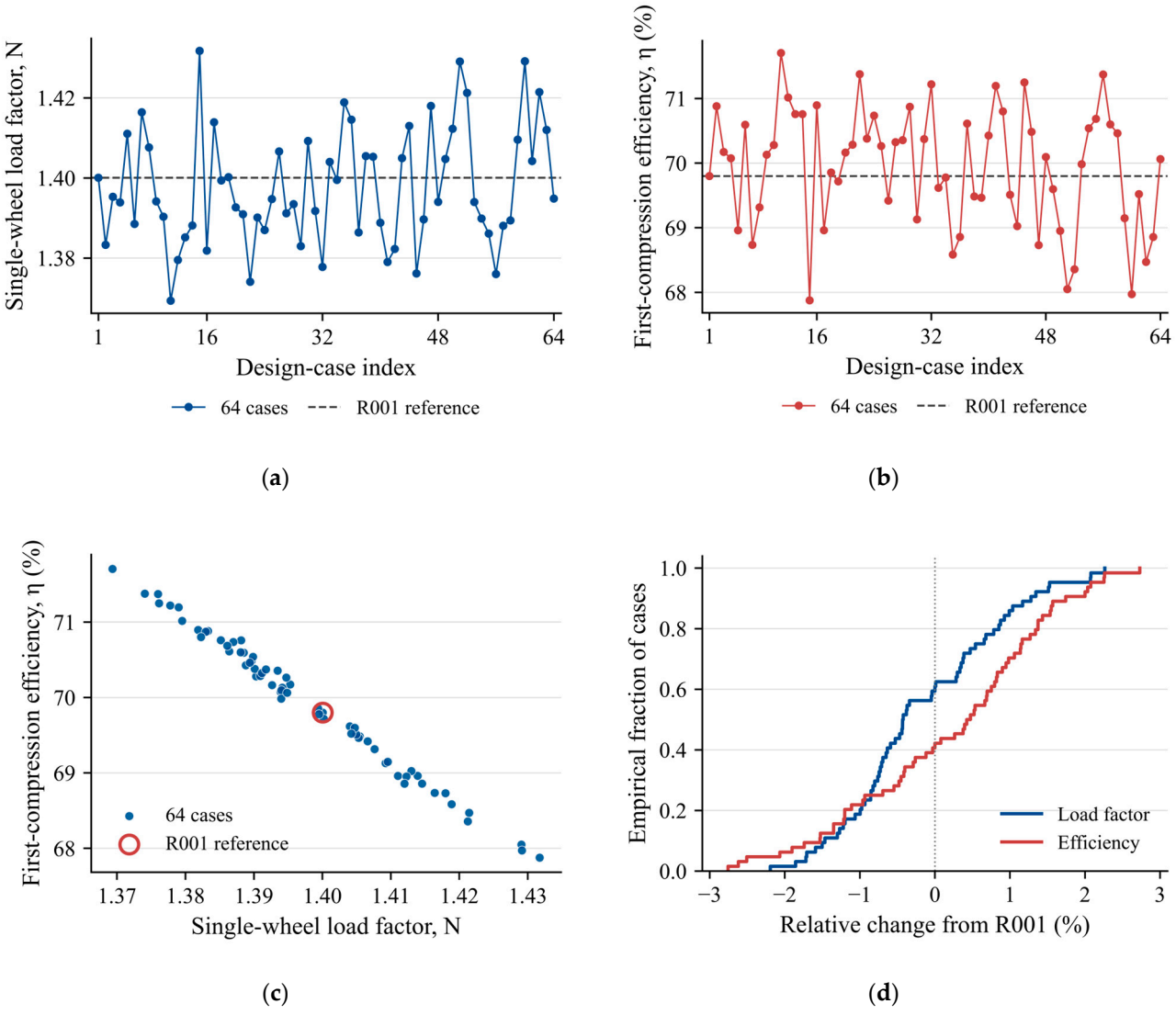


Figure 7. Responses of the 64-case diameter-screening design, evaluated by MAPDL at a 0.5 ms step through first maximum strut compression. (**a**,**b**) Load factor and efficiency in case order. (**c**) Paired responses with the unperturbed baseline, R001, identified. (**d**) Empirical fractions of relative changes from R001 (N = 1.400056 and η = 69.7993%). The prescribed cases form a deterministic design, rather than a manufacturing probability sample.

4.5. Spatial Distribution of Main-Effect Sensitivity

The largest load-factor scores occurred at 150, 160, 170, 140 and 130 mm. Efficiency scores were highest at 150, 160, 140, 170 and 130 mm (Table 4 and Figure 8). The two responses therefore shared the same five leading stations, with a different ordering at 140 and 170 mm. Their complete station rankings had a Spearman coefficient of 0.9675.

The concentration of influential stations around 140–170 mm connects local restriction geometry with the evolving landing response. Each nodal diameter affects both adjacent interpolation intervals and consequently modifies hydraulic resistance over a finite stroke range. The resulting changes in velocity and arm motion contribute to both peak tire load and accumulated strut work. Main-effect scores identify influential regions but do not locate the instantaneous force peak.

Marginal and adjusted analyses gave identical station orderings. The collapsed strength-two design retains pairwise orthogonality between main-effect columns, despite unequal level frequencies. Consequently, both analyses rank the same factor sums of

squares. This algebraic agreement is expected from the design and does not independently demonstrate ranking stability.

The additive models gave $R^2 = 0.999811$ for load factor and 0.999878 for efficiency. With two numerator degrees of freedom per factor and 21 residual degrees of freedom, the orthogonal decomposition satisfies $R^2 = \Sigma Fi/(\Sigma Fi + 21/2)$. The fitted models and the tabulated statistics agree with this identity.

These high R^2 values describe variation within the 64 prescribed combinations. They do not resolve the 210 possible factor pairs or demonstrate prediction accuracy outside the sampled diameter range. Section 4.11 evaluates prediction on independent holdout cases and examines total-order sensitivity under an explicit input distribution.

Close neighboring scores make the detailed ordering less certain than the location of the influential region. Section 4.9 quantifies this sensitivity using residual reallocation and leave-one-case-out fitting. The reported ranges describe stability conditional on the numerical model and design, rather than confidence in a manufacturing population.

Table 4. Adjusted main-effect F statistics, normalized score shares and partial effect sizes for the 21 perturbed axial positions in the 64-case study. Positions are ordered by descending F separately for each response; numerator and residual degrees of freedom are 2 and 21, respectively.

Response	Position (mm)	Adjusted F	Score Share (%)	Partial η^2
Load factor	150	4831.3	8.68	0.9978
Load factor	160	4766.2	8.57	0.9978
Load factor	170	4409.6	7.93	0.9976
Load factor	140	4238.9	7.62	0.9975
Load factor	130	3715.4	6.68	0.9972
Load factor	120	3697.9	6.65	0.9972
Load factor	110	3412.1	6.13	0.9969
Load factor	190	3375.8	6.07	0.9969
Load factor	180	3349.2	6.02	0.9969
Load factor	100	3269.3	5.88	0.9968
Load factor	90	2749.7	4.94	0.9962
Load factor	80	2206.0	3.96	0.9953
Load factor	20	1852.9	3.33	0.9944
Load factor	70	1822.3	3.28	0.9943
Load factor	30	1713.9	3.08	0.9939
Load factor	10	1595.5	2.87	0.9935
Load factor	60	1502.6	2.70	0.9931
Load factor	40	1135.3	2.04	0.9908
Load factor	200	984.1	1.77	0.9894
Load factor	50	768.9	1.38	0.9865
Load factor	0	242.7	0.44	0.9585
Efficiency	150	7984.5	9.28	0.9987
Efficiency	160	7714.2	8.97	0.9986
Efficiency	140	7046.1	8.19	0.9985
Efficiency	170	6922.6	8.05	0.9985
Efficiency	130	6353.2	7.39	0.9984
Efficiency	120	6287.5	7.31	0.9983
Efficiency	110	5636.6	6.55	0.9981
Efficiency	100	5532.9	6.43	0.9981
Efficiency	180	4663.1	5.42	0.9978
Efficiency	90	4637.5	5.39	0.9977
Efficiency	80	3710.5	4.31	0.9972
Efficiency	190	3096.5	3.60	0.9966

Efficiency	70	3082.1	3.58	0.9966
Efficiency	60	2527.2	2.94	0.9959
Efficiency	30	2434.7	2.83	0.9957
Efficiency	20	2379.1	2.77	0.9956
Efficiency	40	1859.7	2.16	0.9944
Efficiency	10	1792.0	2.08	0.9942
Efficiency	50	1381.2	1.61	0.9925
Efficiency	200	759.8	0.88	0.9864
Efficiency	0	212.4	0.25	0.9529

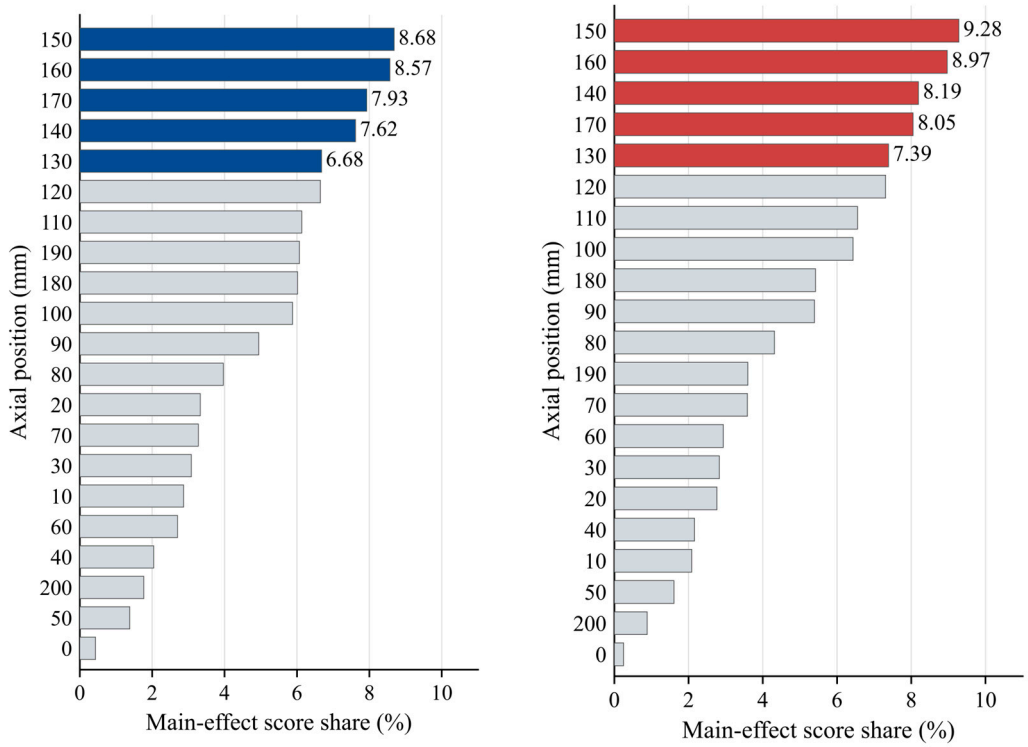


Figure 8. Normalized main-effect scores for all 21 stations in the 64-case dimensional study. (**a**) Single-wheel load factor; (**b**) first-compression efficiency. Stations are sorted separately within each response, with score share = 100Fi/ΣFi.

4.6. Conditional Force Changes Caused by Diameter Errors

Uniform positive and negative diameter errors have asymmetric hydraulic effects (Figure 9). At a 24.0 mm nominal diameter, +0.2 mm produces a local force increase of 23.72%, whereas −0.2 mm produces a decrease of 17.35%. The asymmetry follows from the inverse dependence on the annular area and is reproduced by Equation (13). A linear approximation gives nearly symmetric deviations and becomes less accurate as the restriction narrows.

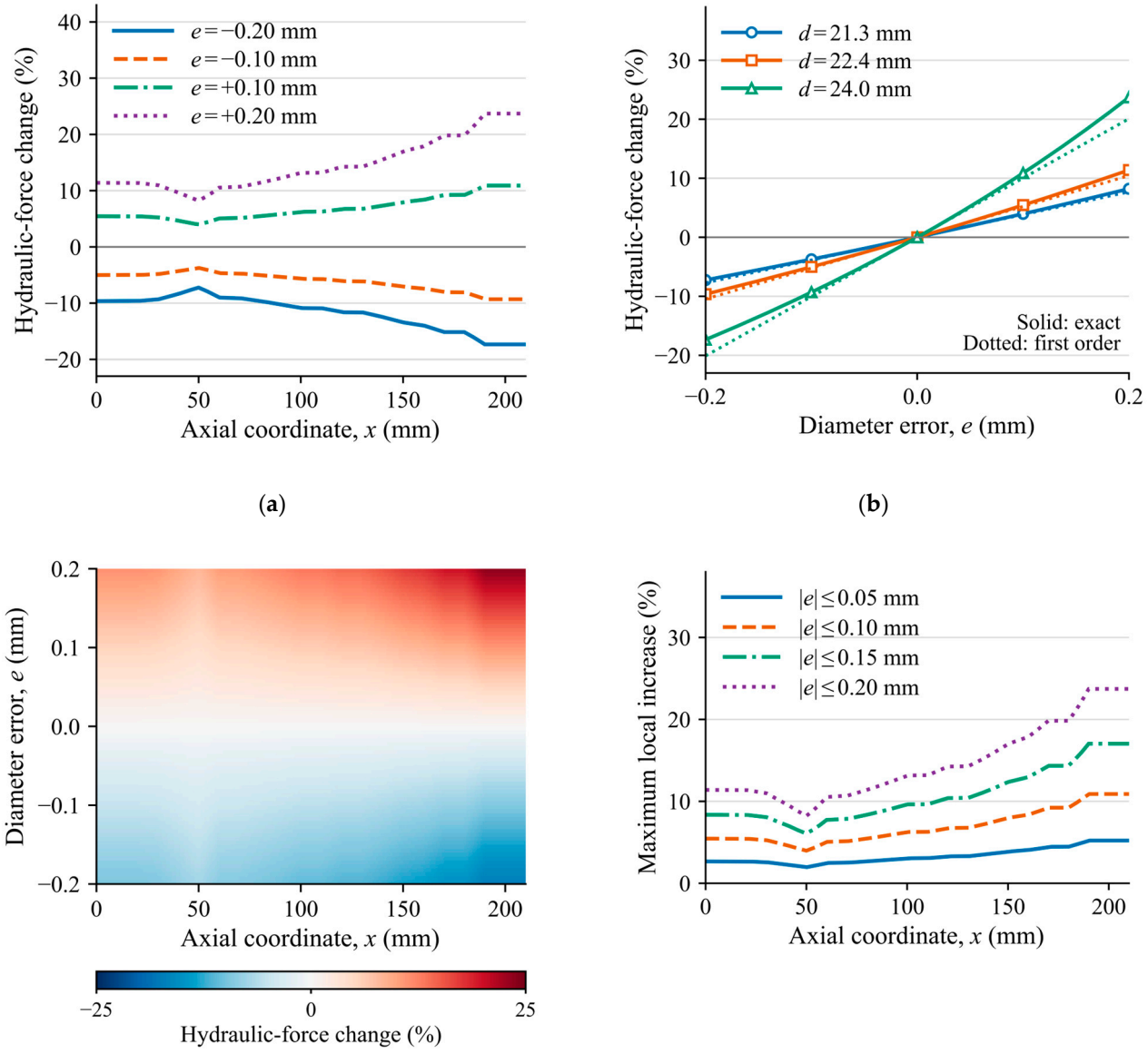


Figure 9. Analytical effects of pin-diameter errors at fixed stroke velocity. (**a**) Relative hydraulic-force changes for four signed diameter errors. (**b**) Exact and first-order responses at three representative diameters. (**c**) Force-change map over axial coordinate and signed diameter error e. (**d**) Maximum local force increase within four symmetric diameter bounds.

The same prescribed diameter offset produces different local force changes along the pin. Amplification is lowest near the 21.3 mm minimum and highest in the larger-diameter tail. At a nominal diameter of 24.0 mm, a symmetric ±0.05 mm scenario gives a maximum local increase of 5.22%, compared with 23.72% for ±0.20 mm. These are fixed-velocity hydraulic calculations, not distributions of manufacturing deviations.

The stronger response to positive errors motivates examining asymmetric diameter-offset scenarios in future validated work. An example such as +0.05/−0.10 mm is an analytical scenario, not a production tolerance. Complete landing response, rebound, correlated geometric errors and measured process capability would be needed to assess such a choice.

Local hydraulic gain and system-level sensitivity characterize different parts of the response. The larger-diameter tail has the strongest fixed-velocity amplification, whereas the leading system-level scores occur around 140–170 mm. The latter incorporate the changing stroke velocity, tire force and arm motion. A dimensional-control assessment therefore requires both the local flow relation and the coupled landing dynamics.

4.7. Objective-Weighted Spatial Priorities

Figure 10 combines the load-factor and efficiency scores using Equation (14). The 150 mm station has the largest normalized score for both objectives and therefore remains first throughout $0 \leq \lambda \leq 1$. Changing the objective weight alters some neighboring ranks without changing the leading station.

The five leading stations remain 130, 140, 150, 160 and 170 mm throughout the weighting interval. Within this group, 140 and 170 mm exchange third and fourth positions at $\lambda = 0.3188$. The analysis therefore identifies a common region of influence while retaining objective-dependent ordering within that region.

At equal weights, the leading order is 150, 160, 170, 140 and 130 mm, accounting for 40.67% of the combined score. Cumulative scores quantify how much of the normalized main-effect total is associated with a selected number of stations. The weights encode a design preference; they do not incorporate manufacturing capability or allowable performance loss. Translating these scores into inspection limits would require those additional inputs.

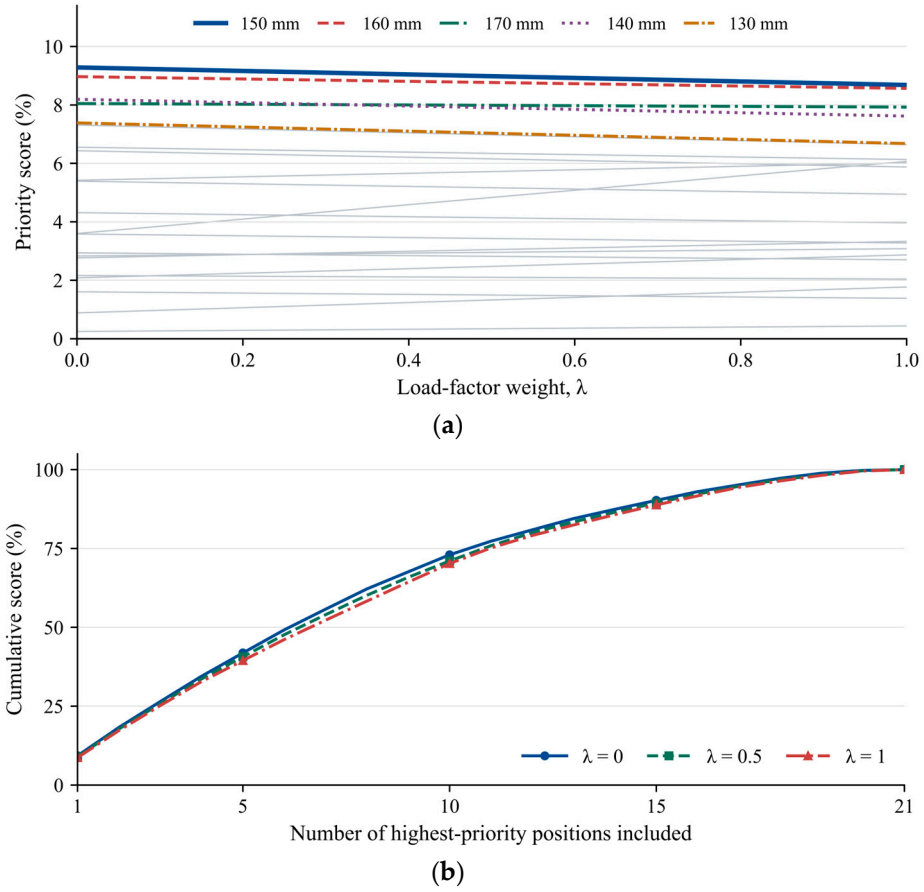


Figure 10. Objective-weighted priorities calculated from Table 4. (**a**) Score functions for all 21 stations, with the common five leading stations highlighted. The 150 mm station leads throughout; 140 and 170 mm exchange third and fourth positions at $\lambda = 0.3188$. (**b**) Cumulative scores after separate ranking at weights 0, 0.5 and 1. The common top-five set accounts for 40.67% at equal weights.

4.8. Model Credibility, Uncertainty and Validation Limits

Published tests support the coupled gas, hydraulic and tire modeling approach, but require assembly-specific calibration. Gan et al. [19] used a polytropic exponent of 1.3 and discharge coefficient of 0.8 in a light-aircraft drop model. Measured strokes of 37.88 and 73.85 mm were compared with predictions of 38.21 and 71.67 mm. Karam and Maré [4] compared predicted and measured chamber pressures for two struts using a richer thermal and gas–oil formulation. Classic vertical-drop comparisons also support gas compression, velocity-squared hydraulic resistance and tire modeling [32]. Table 5 distinguishes this evidence from validation of the present coefficients and geometry.

Table 5. Experimental support for related modeling components and limits of transfer to the present study.

Modeling Component	Published Evidence	Limit of Transfer
Gas and hydraulic strut force	Gan et al. [19]: coupled drop-test comparisons; Karam and Maré [4]: measured/predicted chamber pressures for two struts	Supports the model class; does not identify the present gas area, charge, exponent or discharge coefficient
Gas, hydraulic and tire coupling	Milwitzky and Cook [32]: vertical-drop comparisons with and without tire bottoming	Conditions and geometries differ from the present articulated assembly
Multibody and ground-contact response	Liu et al. [9]: measured ground/axle loads and stroke; parameters calibrated to tests	No transferable error bound or validation of this pin profile
Friction-related behavior	Gan et al. [19]: combined model compared with two test conditions	Does not identify the bearing-friction parameters for this assembly
Detailed orifice flow	Du et al. [20]: numerical two-phase study compared with engineering estimates	Numerical context only; not experimental validation
Articulated twin-wheel model and station ranking	No assembly-specific physical comparison	Numerical verification, algorithm stability and sampling diagnostics remain distinct from physical validation

Liu et al. [9] reported three drop tests at a reduced mass of 13,472 kg and sink speeds of 3.08–3.10 m/s. Their measured efficiencies were 65.9–67.8%, compared with 69.842% and 95.302% for the baseline and optimized profiled pins in this study. The masses and geometries differ. Their load factors of 1.62–1.69 also use reduced-mass weight as the denominator, whereas Equation (8) uses a static single-wheel reference. These differences preclude direct numerical validation through agreement of response magnitudes. The experiments instead support the selected modeling mechanisms and guide assembly-specific validation.

The fixed polytropic exponent $\nu = 1.3$ and discharge coefficient simplify thermal and fluid behavior. At fixed diameter and velocity, Equation (6) makes hydraulic force proportional to oil density and inversely proportional to C_d squared. An illustrative +5% change in C_d reduces this force by 9.30%, while a −5% change increases it by 10.80%. These are algebraic scenarios, not measured uncertainties or recalculated tire-load changes. For net gas force in Equation (7), logarithmic sensitivity to ν is $[p_g/(p_g - p_b)]\ \ln[V_0/(V_0 - A_g s)]$. At 194 mm, $V_0 = 4.6$ L, $p_0 = 2.95$ MPa absolute and $p_b = 0.101325$ MPa, the sensitivity is 1.37555. A ±0.1 change in ν changes net gas force by +14.74%/−12.86% at that fixed stroke. Transient heat exchange, cavitation, aeration and Reynolds-number effects remain unquantified at system level.

The numerical study evaluates nominal optimization and prescribed dimensional variation. Independent uniform offsets in Section 4.11 represent an assumed input distribution, not measured process capability. Robust-design and reliability-based optimiza-

tion [33,34] would require appropriate manufacturing distributions and experimental validation. Correlated geometric errors, friction, gas charge, tire properties and landing conditions may change the response and station ordering.

4.9. Numerical Verification and Ranking Stability

ANSYS Mechanical APDL 2022 R1 implements the two-coordinate twin-wheel equations using the parameters in Table 1. The coordinates represent upper-body vertical displacement and arm rotation, while the strut geometry retains its transverse attachment offset. Both tire forces enter the dynamic balance, and the load factor is evaluated per wheel. Independent ordinary-differential-equation integration provides a numerical comparison for the same governing equations.

The computational model uses the attachment coordinates and mass properties defined in Section 2. The arm center of mass lies halfway between its pivot and the wheel axle, and the tires have identical stiffness and damping. Bearing friction, horizontal tire force, wheel spin and aerodynamic lift are omitted. These assumptions define the scope of the numerical comparison.

The MAPDL time step is 0.5 ms through first maximum strut compression. The extension stop balances the initial net gas force of 50.3402 kN and releases after 0.503402 mm of compression. Its initial stored energy of 12.6707 J is included in the energy balance. MAPDL updates the hydraulic coefficient using the preceding converged stroke, whereas the independent integrator evaluates it at the instantaneous state. Step refinement assesses the resulting discretization difference.

The 64 design cases and four prespecified refinement runs completed without solver errors. The maximum energy residual was 0.1435% of initial kinetic energy; vertical-momentum and hydraulic-identity residuals were 0.00816 and 0.02545 N. Halving the time step changed five response metrics by at most 0.03021%. Differences from independent DOP853 integration were at most 0.06554%, decreasing to 0.03535% after refinement.

The 64-case responses covered N = 1.36935–1.43174, η = 67.876–71.705% and maximum compression of 200.707–202.721 mm. These responses underlie the station statistics in Table 4. Table 6 and Figure 11 report the stability of the ten highest-ranked stations for each objective, complementing their score magnitudes.

Ranking stability was assessed with 5000 fixed-design residual reallocations and 64 leave-one-case-out fits. Centered, leverage-adjusted residuals were resampled in common rows to preserve pairing between the responses. At 150 mm, the empirical 95% rank range was [1, 2] for both objectives, and leave-one-out ranks ranged from 1 to 3. This station remained in the top five in every replicate of both diagnostics. The ranges assume exchangeable residuals and may not fully represent structured interactions in deterministic simulations. Ordinary row resampling produced rank-deficient fits in 1639 of 2000 draws, motivating the fixed-design analysis. Section 4.11 provides a complementary assessment based on input sampling.

Table 6. Rank stability for the ten highest main-effect stations in each response. The 95% ranges use 5000 fixed-design residual reallocations; leave-one-out ranges use 64 case omissions.

Objective	Position (mm)	95% Rank Range	Leave-One-Out Range
Load factor	150	[1, 2]	1–3
Load factor	160	[1, 2]	1–3
Load factor	170	[3, 4]	1–4
Load factor	140	[3, 4]	3–4
Load factor	130	[5, 6]	5–9
Load factor	120	[5, 6]	5–9
Load factor	110	[7, 10]	5–10

Load factor	190	[7, 10]	5–10
Load factor	180	[7, 10]	5–10
Load factor	100	[7, 10]	6–10
Efficiency	150	[1, 2]	1–3
Efficiency	160	[1, 2]	1–4
Efficiency	140	[3, 4]	2–4
Efficiency	170	[3, 4]	2–6
Efficiency	130	[5, 6]	3–7
Efficiency	120	[5, 6]	3–7
Efficiency	110	[7, 8]	6–8
Efficiency	100	[7, 8]	6–8
Efficiency	180	[9, 10]	9–10
Efficiency	90	[9, 10]	9–10

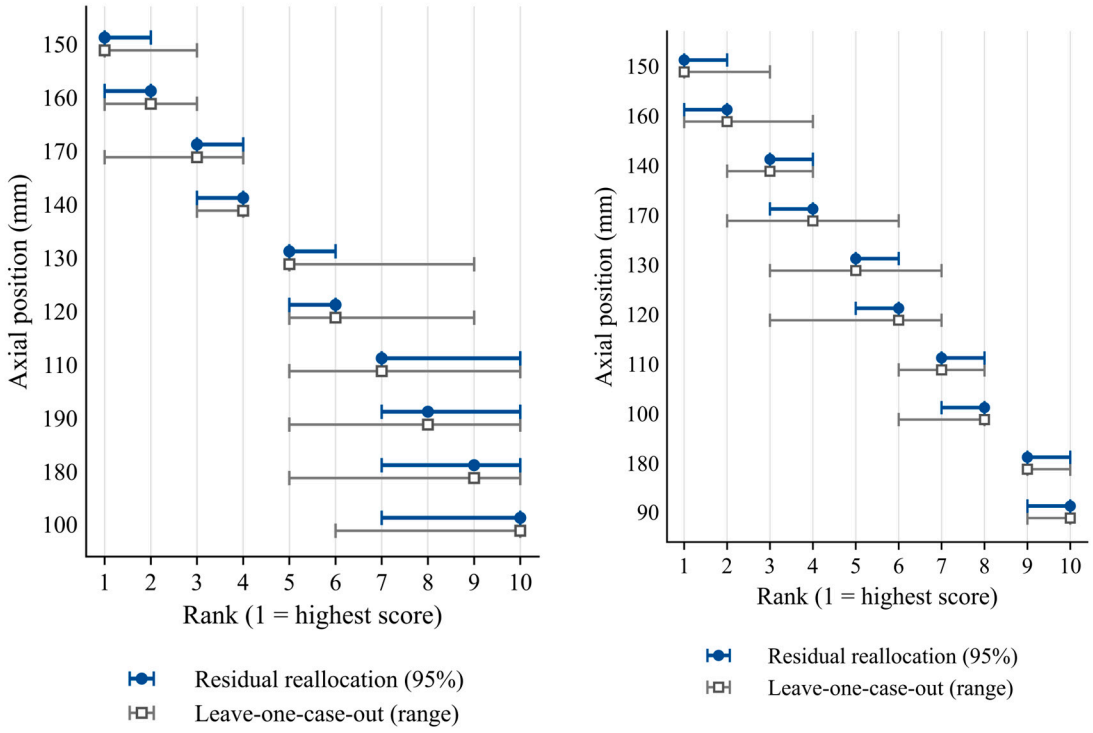


Figure 11. Rank stability for the ten highest main-effect stations in each response. (**a**) Single-wheel load factor; (**b**) first-compression efficiency. Points show fitted ranks. Colored intervals show descriptive 95% ranges from 5000 fixed-design residual reallocations, and gray intervals show the ranges across 64 leave-one-case-out fits.

4.10. Optimization Repeatability and Convergence

Fourth-order Runge–Kutta (RK4) integration used a 0.1 ms step, with event localization and force-peak checks at profile nodes. Across 13 valid benchmark profiles, maximum relative differences from high-accuracy DOP853 solutions were 1.093×10^{-5} in N, 1.236×10^{-6} in η and 8.348×10^{-7} in stroke. Of 380,000 optimization evaluations, 13 failed the declared admissibility checks and received penalties. These candidates were excluded from feasible fronts. Re-evaluation of all 1080 final-front points at half the step provided a further integration check.

Five independent NSGA-II runs used seeds 101, 202, 303, 404 and 505, 22 bounded diameter variables (20–25 mm), population 100 and 200 evaluated generations. Binary dominance/crowding tournaments, simulated-binary crossover and polynomial mutation were used; crossover probability was 0.9 and mutation probability was 0.125 per variable. The treatment of candidates that failed the admissibility checks is summarized above. Load factor and $1 - \eta$ were minimized; the performance targets were assessed after the search rather than imposed as feasibility constraints.

Hypervolume uses fixed normalized objectives ($N/5$, $1 - \eta$) and reference (1,1), corresponding to $N = 5$ and $\eta = 0$. Generation-200 hypervolume is 0.74028 ± 0.00445 (mean ± sample standard deviation), with coefficient of variation 0.60%. Gains over the final 50 generations are 0.261–1.240%. Extending the five seeded runs to 400 evaluated generations yields further gains of 0.210–1.200% (Table 7; Figure 12). These remaining gains preclude a claim of full Pareto convergence.

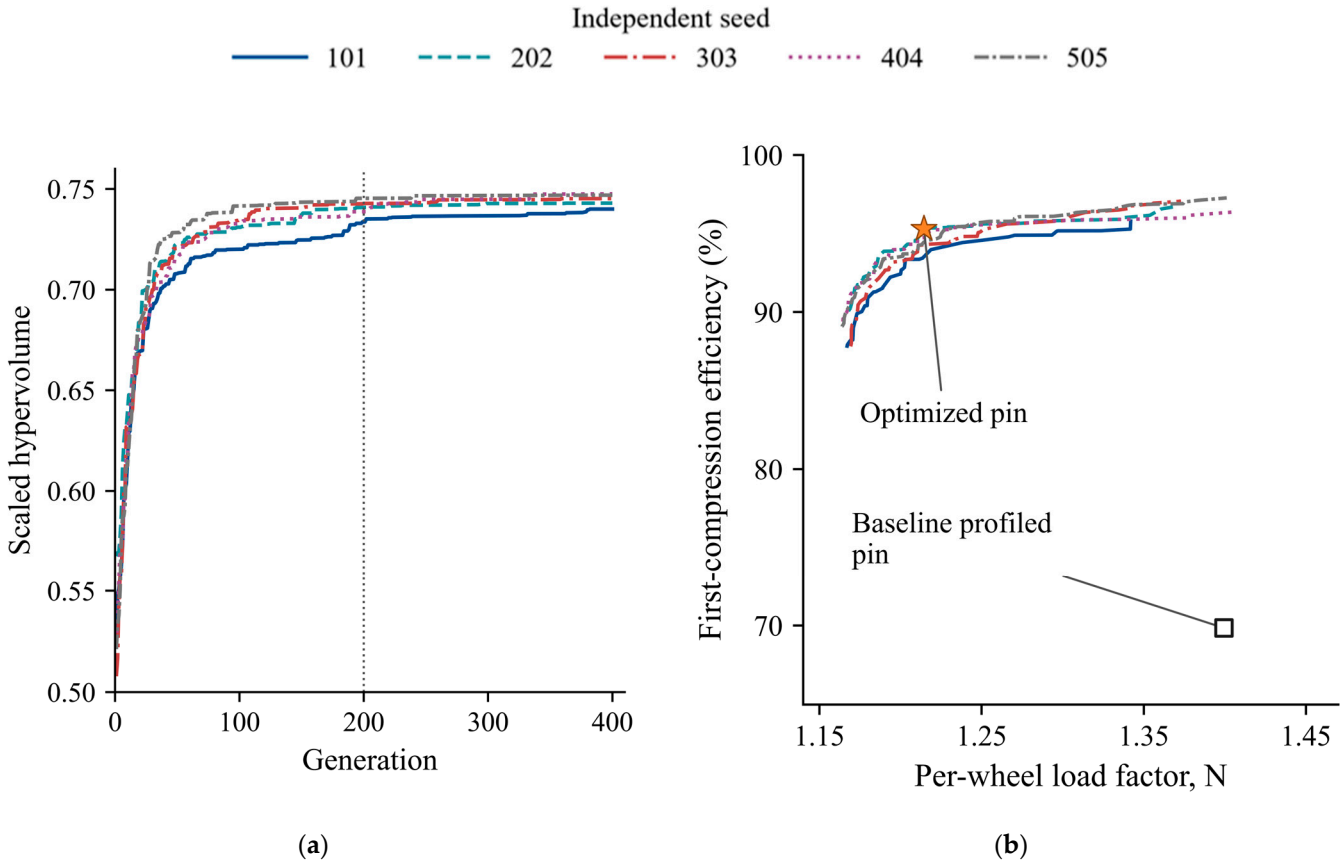


Figure 12. Optimization repeatability and convergence diagnostics. (**a**) Fixed-reference hypervolume histories for five seeds and their 400-generation extensions; (**b**) generation-200 nondominated sets with the baseline profiled pin. The objectives use the first-compression window defined in Section 2.4. Table 3 separately reports the 0–2 s load-factor checks for the three representative designs.

At the same 20,000-evaluation budget and seed 101, lowering crossover probability to 0.8, setting mutation probability to 0.05 or 0.25, and using population 200 for 100 evaluated generations change final hypervolume by +1.186%, +0.916%, +1.067% and +0.805%, respectively. These one-factor comparisons test local algorithm sensitivity; they are not replicated searches across all parameter combinations.

The optimized pin was selected from the pooled nondominated sets of five 200-generation runs. Selection minimized Euclidean distance to the componentwise ideal after ideal-to-nadir scaling. Independent integration gave $N = 1.214471$, $\eta = 95.302\%$ and maximum compression of 187.646 mm. The 0–2 s load factor was also 1.214471, meeting both

numerical design targets. The minimum N among the five generation-200 fronts was 1.164105, illustrating the trade-off represented by the selected compromise. At its maximum stroke, the 200 and 210 mm nodes are inactive and cannot be identified uniquely from these objectives.

Table 7. Hypervolume (HV) diagnostics for five independent twin-wheel optimization runs. Each extension repeats the same seeded first 200 generations before continuing to 400.

Seed	HV at 200	HV at 400	Gain (%)
101	0.733651	0.740036	0.870
202	0.740822	0.742980	0.291
303	0.742822	0.745233	0.324
404	0.738714	0.747576	1.200
505	0.745374	0.746941	0.210

4.11. Interaction-Aware Sensitivity and Independent Prediction Checks

The global sensitivity study varied the 21 diameters from 0 to 200 mm independently and uniformly within ±0.2 mm of the baseline profile. The 210 mm endpoint remained fixed. Because baseline compression exceeds 200 mm, this endpoint participates in the last interpolation interval despite being excluded as a varied factor. The distribution defines an analytical scenario. A scrambled Sobol design with seed 20261101 used 2048 paired base rows and 21 pick-freeze hybrids, giving 47,104 dynamic evaluations. Jansen total-order estimates include contributions from each factor and its interactions [35].

The five largest total-order estimates occurred at 150, 160, 170, 140 and 120 mm for load factor. For efficiency, the corresponding order was 150, 160, 140, 170 and 120 mm (Figure 13). Paired-row resampling with 2000 replicates gave descriptive 95% rank ranges of [1, 3] and [1, 2] at 150 mm, respectively. These ranges characterize sampling stability within one scrambled low-discrepancy design; calibrated confidence coverage is not established. The leading four stations agree with the 64-case main-effect analysis, while the fifth is 120 mm rather than 130 mm.

Independent Latin-hypercube designs provide 2048 training and 1024 holdout cases, bringing the sensitivity study to 50,176 dynamic evaluations, all valid. The 43-parameter additive quadratic model gives holdout $R^2 = 0.999670$ for load factor and 0.999709 for efficiency. Adding all 210 bilinear interactions raises these to 0.99999796 and 0.99999859. Load-factor root-mean-square error (RMSE) decreases from 0.0002173 to 0.00001708, and efficiency RMSE from 0.012943 to 0.000900 percentage points. Interactions therefore improve prediction within the assumed input box, although the additive model already explains most variation. Finite-sample first-order estimates slightly exceed total-order estimates and sum above one; their differences are not used to assign precise interaction fractions.

Both analyses identify a leading region around 140–170 mm under the prescribed drop condition. Their different fifth-ranked stations show that detailed priorities depend on the sensitivity definition and sampling design. These rankings remain conditional on the contact law, gas model, mass properties and independent diameter offsets. Correlated manufacturing deviations and different landing conditions require separate assessment. Spatial sensitivity was evaluated around the baseline profiled pin, whereas the optimized pin was assessed for nominal landing performance.

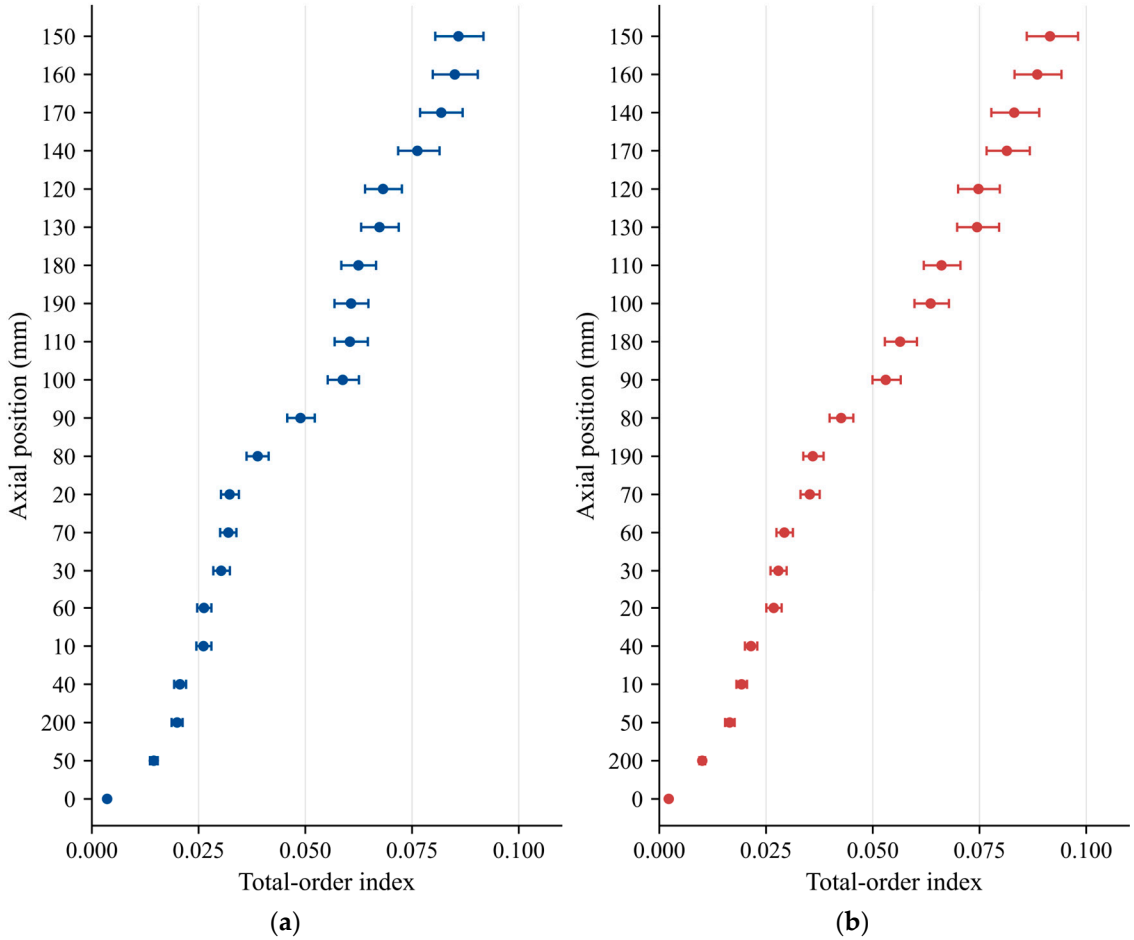


Figure 13. Total-order sensitivity under independent uniform diameter offsets, evaluated over the first-compression response. (**a**) Single-wheel load factor; (**b**) efficiency. Horizontal intervals show descriptive 95% paired-row bootstrap ranges from one scrambled Sobol design.

5. Conclusions

Metering-pin optimization reduced the 0–2 s single-wheel load factor to 1.21447 and increased first-compression efficiency to 95.302% for the prescribed twin-wheel drop condition. The optimized pin satisfied $N \leq 1.9$ and $\eta \geq 0.80$. Relative to the constant pin, the load factor decreased by 25.40% and efficiency increased by 38.03 percentage points.

At unchanged velocity, +0.2 and −0.2 mm offsets at a nominal diameter of 24.0 mm produce hydraulic-force changes of +23.72% and −17.35%. This asymmetry motivates further examination of diameter-error direction; it does not specify a manufacturable tolerance or acceptable component limit.

The 64-case main-effect and total-order analyses identified a common influential region around 140–170 mm, with differences in neighboring station ranks. The 150 mm station led both main-effect score distributions and remained first across all convex objective weights. Analytical diameter gain, system-level scores and rank diagnostics together provide a basis for conditional spatial screening.

Independent integration, time-step refinement and repeated optimization runs supported numerical reproducibility. Residual hypervolume improvements with a larger generation budget indicate that global convergence remains unestablished. Assembly-specific drop tests, characterization of correlated geometric deviations and manufacturing-capability measurements are required before numerical priorities can inform production acceptance limits.

Author Contributions: Conceptualization, K.W. and Q.Z.; methodology, K.W. and X.Z.; software, K.W. and Q.Z.; validation, K.W. and Q.Z.; formal analysis, K.W. and Q.Z.; investigation, K.W., X.Z., Q.Z. and W.Z.; writing—original draft preparation, K.W., X.Z. and Q.Z.; writing—review and editing, K.W., X.Z. and Q.Z.; supervision, W.Z. All authors have read and agreed to the published version of the manuscript.

Funding: This work was supported by the project of China Ship Scientific Research Center(grant number 452500001K6104GA01).

Institutional Review Board Statement: Not applicable.

Informed Consent Statement: Not applicable.

Data Availability Statement: The model inputs and summarized numerical results reported in this study are included in the article.

Acknowledgments: The authors thank the laboratory members for their assistance during the experiments.

Conflicts of Interest: The authors declare no conflicts of interest.

Nomenclature

Symbol	Definition	Unit
r_i, r_i^P, θ_i, ρ_i^P	Body reference/point position, planar angle and body-fixed attachment vector	m; m; rad; m
m_i, g, t	Body mass, gravitational acceleration and time	kg; m/s^2; s
R, **q**, **M**, **Φ**, **μ**, **Q**	Rotation matrix, coordinates, mass matrix, constraints, reaction multipliers and generalized forces	As defined in Equations (1) and (2)
h, $l_\perp$, l, l_0	Projected attachment separation, transverse offset, current and initial strut lengths	m
s, $\dot{s}$, s_{max}	Compression, compression velocity and first-compression maximum	m; m/s; m
x, x_i, $d(x)$, d_i	Axial coordinate, node coordinate, continuous pin diameter and nodal diameter	mm in profile tables; m in force laws
D_o, D_1, D_2	Metering-hole, outer-cylinder and inner-cylinder diameters	m
A_o, A_h, A_g	Annular flow, displaced-fluid and gas-force areas	m^2
ρ, C_d, β	Oil density, discharge coefficient and hole-to-upstream diameter ratio	kg/m^3; dimensionless; dimensionless
R_h	Hydraulic coefficient multiplying $\dot{s}\|\dot{s}\|$	N·s^2/m^2
F_s, F_g, F_h, F_{stop}	Total axial strut, net gas, hydraulic and opposing extension-stop forces	N
p_0, p_g, p_b, V_0, ν, K_g	Initial and instantaneous absolute gas pressures, external back pressure, initial gas volume, polytropic exponent, tangent gas stiffness	Pa, Pa, Pa, m^3, –, N/m
F_t, $F_{t,total}$, $F_{t,static}$, $F_{s,max}$	Single-wheel tire force, sum of two tire forces, static single-wheel reference and first-compression peak strut force	N
δ	Single-wheel tire compression plotted in Figure 6c	mm
N, η	Single-wheel tire-force factor in the stated window and first-compression energy-utilization efficiency	Dimensionless; η also reported as %
$F_{i,y}$, $w_{i,y}$, $\eta^2_{p,i,y}$	ANOVA F statistic, normalized main-effect score and partial effect size	Dimensionless
e, G_d	Signed pin-diameter error and logarithmic hydraulic diameter gain	mm or m consistently; dimensionless
J_i, λ	Inspection-priority score and load-factor weight	Dimensionless

References

1. Pritchard, J. Overview of Landing Gear Dynamics. *J. Aircr.* **2001**, *38*, 130–137.
2. Krüger, W.R.; Morandini, M. Recent developments at the numerical simulation of landing gear dynamics. *CEAS Aeronaut. J.* **2011**, *1*, 55–68.

3. Pecora, R. A Rational Numerical Method for Simulation of Drop-Impact Dynamics of Oleo-Pneumatic Landing Gear. *Appl. Sci.* **2021**, *11*, 4136.
4. Karam, W.; Maré, J.-C. Advanced model development and validation of landing gear shock struts. *Proc. Inst. Mech. Eng. Part G J. Aerosp. Eng.* **2010**, *224*, 575–586.
5. Lyle, K.H.; Jackson, K.E.; Fasanella, E.L. Simulation of Aircraft Landing Gears with a Nonlinear Dynamic Finite Element Code. *J. Aircr.* **2002**, *39*, 142–147.
6. Lernbeiss, R.; Plöchl, M. Simulation model of an aircraft landing gear considering elastic properties of the shock absorber. *Proc. Inst. Mech. Eng. Part K J. Multi-Body Dyn.* **2007**, *221*, 77–86.
7. Liu, W.; Wang, Y. Improved Multi-Body Dynamic Simulation of Landing Gear Drop Test Incorporating Structural Flexibility and Bearing Contact. *Aerospace* **2024**, *11*, 543.
8. Delprete, C.; Dagna, A.; Brusa, E. Model-Based Design of Aircraft Landing Gear System. *Appl. Sci.* **2023**, *13*, 11465.
9. Liu, W.; Wang, Y.; Ji, Y. Landing Impact Load Analysis and Validation of a Civil Aircraft Nose Landing Gear. *Aerospace* **2023**, *10*, 953.
10. Fan, R.; Fang, Y.; Han, Y.; Xue, C.; Wang, E. Landing dynamic simulation of aircraft landing gear with multi-struts. *J. Vibroeng.* **2014**, *16*, 2494–2507.
11. Xue, C.J.; Han, Y.; Qi, W.G.; Dai, J.H. Landing-Gear Drop-Test Rig Development and Application for Light Airplanes. *J. Aircr.* **2012**, *49*, 2064–2076.
12. Kong, J.P.; Lee, Y.S.; Han, J.D.; Ahn, O.S. Drop impact analysis of smart unmanned aerial vehicle (SUAV) landing gear and comparison with experimental data. *Mater. Und Werkst.* **2009**, *40*, 192–197.
13. Fang, W.; Zhu, L.; Wang, Y. Landing Performance Study for Four Wheels Twin Tandem Landing Gear Based on Drop Test. *Aerospace* **2022**, *9*, 334.
14. Shi, F. Multi-objective Optimization of Passive Shock Absorber for Landing Gear. *Am. J. Mech. Eng.* **2019**, *7*, 79–86.
15. Dinç, A. Metering pin diameter optimization of an aircraft landing gear shock absorber. *Eskişeh. Tek. Üniversitesi Bilim Ve Teknol. Derg. B-Teor. Bilim.* **2021**, *9*, 37–46.
16. Liu, W.; Zhao, B.; Pan, X.; Song, Z.; Wang, P. Modeling of the Nose Landing Gear Shock Absorber for Carrier-Based Aircraft and Optimization of Oil Orifice Area Configuration. *Fluids* **2025**, *10*, 285.
17. Ghiringhelli, G.L. Testing of Semiactive Landing Gear Control for a General Aviation Aircraft. *J. Aircr.* **2000**, *37*, 606–616.
18. Kang, B.H.; Jo, B.H.; Kim, B.G.; Hwang, J.H.; Choi, S.B. Linear and Nonlinear Models for Drop Simulation of an Aircraft Landing Gear System with MR Dampers. *Actuators* **2023**, *12*, 287.
19. Gan, S.; Fang, X.; Wei, X. Parametric Analysis on Landing Gear Strut Friction of Light Aircraft for Touchdown Performance. *Appl. Sci.* **2021**, *11*, 5445.
20. Du, S.; Zhang, C.; Zhou, K.; Zhao, Z. Study of the Two-Phase Flow Characteristics of a Damping Orifice in an Oleo-Pneumatic Shock Absorber. *Fluids* **2022**, *7*, 360.
21. Zhang, L.; Nie, H.; Wei, X. Tolerance Design and Robust Study for The Joint Clearances of Landing Gear Retraction Mechanisms. *Appl. Sci.* **2020**, *10*, 4856.
22. Pinello, L.; Hassan, O.; Giglio, M.; Sbarufatti, C. Preliminary Nose Landing Gear Digital Twin for Damage Detection. *Aerospace* **2024**, *11*, 222.
23. Li, F.; Zhu, J.; Zou, X.; Pan, Z.; Chen, J. Multibody Analysis of Lever-Spring Landing Gear with Elastomer Shock Absorbers: Modelling, Simulations and Drop Tests. *Aerospace* **2025**, *12*, 367.
24. Deb, K.; Pratap, A.; Agarwal, S.; Meyarivan, T. A fast and elitist multiobjective genetic algorithm: NSGA-II. *IEEE Trans. Evol. Comput.* **2002**, *6*, 182–197.
25. Gomes, C.; Thule, C.; Broman, D.; Larsen, P.G.; Vangheluwe, H. Co-Simulation: A Survey. *ACM Comput. Surv.* **2018**, *51*, 49.
26. Sacks, J.; Welch, W.J.; Mitchell, T.J.; Wynn, H.P. Design and Analysis of Computer Experiments. *Stat. Sci.* **1989**, *4*, 409–423.
27. Lakens, D. Calculating and reporting effect sizes to facilitate cumulative science: A practical primer for t-tests and ANOVAs. *Front. Psychol.* **2013**, *4*, 863.
28. Sobol', I.M. Global sensitivity indices for nonlinear mathematical models and their Monte Carlo estimates. *Math. Comput. Simul.* **2001**, *55*, 271–280.
29. Saltelli, A.; Annoni, P.; Azzini, I.; Campolongo, F.; Ratto, M.; Tarantola, S. Variance based sensitivity analysis of model output. Design and estimator for the total sensitivity index. *Comput. Phys. Commun.* **2010**, *181*, 259–270.
30. Morris, M.D. Factorial Sampling Plans for Preliminary Computational Experiments. *Technometrics* **1991**, *33*, 161–174.

31. Campolongo, F.; Cariboni, J.; Saltelli, A. An effective screening design for sensitivity analysis of large models. *Environ. Model. Softw.* **2007**, *22*, 1509–1518.
32. Milwitzky, B.; Cook, F.E. *Analysis of Landing-Gear Behavior*; NACA Report 1154; NASA: Washington, DC, USA, 1953.
33. Krüger, J.C.; Kranz, M.; Schmidt, T.; Seifried, R.; Kriegesmann, B. An efficient and non-intrusive approach for robust design optimization with the first-order second-moment method. *Comput. Methods Appl. Mech. Eng.* **2023**, *414*, 116136.
34. Hu, W.; Cheng, S.; Yan, J.; Cheng, J.; Peng, X.; Cho, H.; Lee, I. Reliability-based design optimization: A state-of-the-art review of its methodologies, applications, and challenges. *Struct. Multidiscip. Optim.* **2024**, *67*, 168.
35. Jansen, M.J.W. Analysis of variance designs for model output. *Comput. Phys. Commun.* **1999**, *117*, 35–43.

Disclaimer/Publisher's Note: The statements, opinions and data contained in all publications are solely those of the individual author(s) and contributor(s) and not of MDPI and/or the editor(s). MDPI and/or the editor(s) disclaim responsibility for any injury to people or property resulting from any ideas, methods, instructions or products referred to in the content.